Lawrence Berkeley National Laboratory
LBL Publications

Title

An international model comparison study of controlled fault activation experiments in argillaceous claystone at the Mont Terri Laboratory

Permalink

https://escholarship.org/uc/item/5wb3k4tk

Authors

Rutqvist, Jonny
Graupner, Bastian
Guglielmi, Yves
et al.

Publication Date

2020-12-01

DOI

10.1016/j.ijrmms.2020.104505

Peer reviewed

An international model comparison study of controlled fault activation experiments in argillaceous claystone at the Mont Terri Laboratory

Jonny Rutqvist [a,*], Bastian Graupner [b], Yves Guglielmi [a], Taehyun Kim [c], Jobst Maßmann [d], Thanh Son Nguyen [e], Jung-Wook Park [c], Wenjie Shiu [f], Luca Urpi [g], Jeoung Seok Yoon [h], Gesa Ziefle [d], Jens Birkholzer [a]

[a] Lawrence Berkeley National Laboratory, Berkeley (LBNL), USA
[b] Swiss Federal Nuclear Safety Inspectorate (ENSI), Brugg, Switzerland
[c] Korea Institute of Geoscience and Mineral Resources (KIGAM), South Korea
[d] Federal Institute for Geosciences and Natural Resources (BGR), Hanover, Germany
[e] Canadian Nuclear Safety Commission (CNSC), Ottawa, Canada
[f] SINOTECH Engineering Consultants, INC, Taiwan
[g] Swiss Seismological Service (SED), Zurich, Switzerland
[h] DynaFrax UG, Potsdam, Berlin, Germany

ABSTRACT

We present results from an international model comparison study involving a series of controlled fault activation experiments in Opalinus Clay at the Mont Terri Laboratory, Switzerland. The fault activation experiments were conducted in situ by water injection at variable pressure from boreholes targeting different parts of the Main Fault crossing several tunnels and galleries of the Mont Terri Laboratory. The model simulations focused on (1) an experiment activating a discontinuity (fracture or minor fault) within the damage zone of the main fault, and (2) an experiment activating discontinuities close to the core of the Main Fault. The experimental data consist of coupled hydraulic and mechanical responses monitored at an injection borehole and a monitoring borehole located a few meters away. After overcoming several modeling issues along with necessary model developments, a reasonably good agreement was achieved between the modeling results and the field observations. The fault activation experiments displayed an abrupt flow rate increase associated with a sudden fracture opening and rupture propagation after the injection pressure reached above the estimated normal stress on the fracture. This was followed by an abrupt flow rate decrease, indicating hydraulic closing, once the injection pressure decreases to an estimated 1–2 MPa below the stress normal to the opened fracture. The models were able to capture this abrupt hydromechanical behavior, including an observed dominant opening behavior along with the rupture propagation, while the spatial extent of the shear rupture and the quantity of peak injection flow were the most challenging to predict.

1. Introduction

The potential for activation of faults and fractures in low permeability argillaceous (compacted) claystone or shale is relevant to a number of geo-energy activities, such as to ensure caprock integrity of geologic sequestration sites,[1] for improved stimulation and production from shale gas reservoirs,[2–4] and for safe permanent geologic disposal of nuclear waste in argillaceous clay formations.[5] The main concern associated with nuclear waste disposal is the potential for repository induced or natural perturbations to create permeable flow paths through the initially impermeable host rock barrier. If such a flow path is created and remains open permanently, it could provide a transport path for radionuclides if released from a waste package.

In geologic nuclear waste disposal in argillaceous clay, fault activation may be caused by repository-scale thermally-driven stress changes and so-called thermal pressurization.[6,7] Thermal pressurization is a process of pressure increase by thermal expansion of pore-fluids trapped within pores of the low permeability host rock (Fig. 1). If not carefully

managed by an appropriate repository design, the repository temperature and associated thermal pressurization could become so high that it could potentially cause hydraulic fracturing or shear activation of existing fractures and minor faults.[8] The impact of such thermal pressurization with respect to shear activation is two-fold in that it can (1) reduce the effective stress and shear strength of fractures (or faults), and (2) increase the shear stress across fractures (or faults) (Fig. 1). Other potential causes of fault activation or fracturing of a low permeability host rock include gas generation within the engineered barrier system of a repository[9] or seismic motion from a distant earthquake.[10] Distant earthquakes produce dynamic strains that give rise to pore pressure changes[11] that could potentially trigger shear slip on faults that are stressed near instability.[12]

In this article we present results from an international modeling comparison study of controlled fault activation experiments that were conducted in Opalinus Clay at the Mont Terri Laboratory, Switzerland.[13–15] The study was part of the international collaborative project DECOVALEX-2019 (from 2015 to 2019) where it was denoted Task B.[16] While this article aims at synthesizing some of the most important results and findings related to interpretive modeling of observed hydromechanical fault behavior, a complete coverage of all the results and model comparisons are reported in Graupner et al.[17] In the next section of this article, we introduce the DECOVALEX-2019 Task B, the international modeling teams and their models. This is followed by results from an initial benchmark model exercise, before presenting the modeling of two controlled fault activation experiments at Mont Terri. We end with a discussion on the results and conclusions with implications to nuclear waste disposal in argillaceous clay formations.

2. DECOVALEX-2019 TASK B description

The objectives of DECOVALEX-2019, Task B, were to develop, compare and validate models for fault hydromechanical behavior in argillaceous clay (shale) formations, relevant to deep underground nuclear waste disposal.[16,17] The main task was to develop models and perform interpretative modeling of water-injection fault activation experiments at the Mont Terri Laboratory. The model simulations focused on (1) one experiment activating a discontinuity (fracture or minor fault) within the damage zone of the Main Fault, and (2) a second experiment activating discontinuities close to the core of the Main Fault. The experimental data from these fault activation experiments consist of flow, pore pressure and three-dimensional fault displacement continuously monitored at an injection borehole and a monitoring borehole located a few meters away.

In DECOVALEX-2019, Task B, the modeling teams were tasked to conduct modeling in three steps of increasing complexity:

- Step 1 - Model inception and benchmarking using a simplified setup

- Step 2 - Modeling fault activation experiment in the fault damage zone, and
- Step 3 - Modeling fault activation experiment at the fault core

The Step 1 benchmarking involved modeling of a single discontinuity, a simplified version of the Step 2 fault activation experiment, whereas Step 3 involved modeling of several connected discontinuities. Here we use the term discontinuity as a general term that includes fractures, faults (fractures or discontinuities with previous shear offset), bedding planes, as well as interfaces between rock units, such as the discontinuity that may exist between a fault core and surround rock.

The objective of Step 1 was to provide modeling teams with a well-defined benchmark exercise considering a detailed specification of the discontinuity plane, including a pre-defined hydromechanical model with clearly specified material properties and model geometry. This was intended as a model inception for the modeling teams to familiarize themselves with the problem and allow for necessary model developments and testing. During the course of the three-year project (2015–2019), more benchmarks were defined, including uncoupled flow problems that were used to help the teams identifying technical issues with their models.[17]

Step 2 and 3 were focused on interpretative modeling of the actual field experiments and in addition to providing model valuation they are modeled to advance our understanding of fault activation processes based on measured data. Both of these experiments involved activation of discontinuities at the scale of a few meters, within the Main Fault (Fig. 2). The activation experiments were carried out by water injection into isolated borehole sections (2.4 m in length) that were intersected by a number of discontinuities of various types and orientations. These boreholes were drilled vertically downward from a tunnel in the Mont Terri Laboratory, with the borehole test sections far enough away from the tunnel to avoid any related stress perturbation. Stepwise increases in borehole pressure were imposed until the pressure was sufficiently high to cause an activation of one or several of the discontinuities. Injection rate, fluid pressure and three-dimensional borehole deformations were measured at high frequency with a specialized borehole monitoring equipment.[13,14,18] A protocol for measurements with this borehole monitoring equipment was described in Guglielmi et al.[18] The protocol was presented as an International Society of Rock Mechanics (ISRM) suggested method for step-rate injection method for fracture in-situ properties (SIMFIP). The two fault activation experiments are further described in Sections 5 and 6 related to the Step 2 and Step 3 modeling activities.

3. Modeling teams and numerical simulators

Seven modeling teams of the DECOVALEX-2019 initiative participated in analyzing the experimental data using different modeling
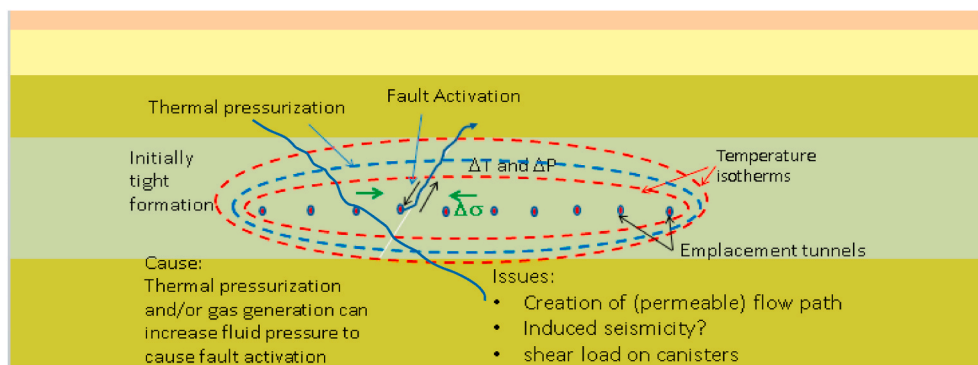

Fig. 1. Conceptual model of a nuclear waste repository in low permeability argillaceous claystone where the heating of the rock mass induces thermal stress and thermal pressurization that could activated faults and fractures and thereby potentially create a permeable flow path for transport of radionuclides if released from a waste package.
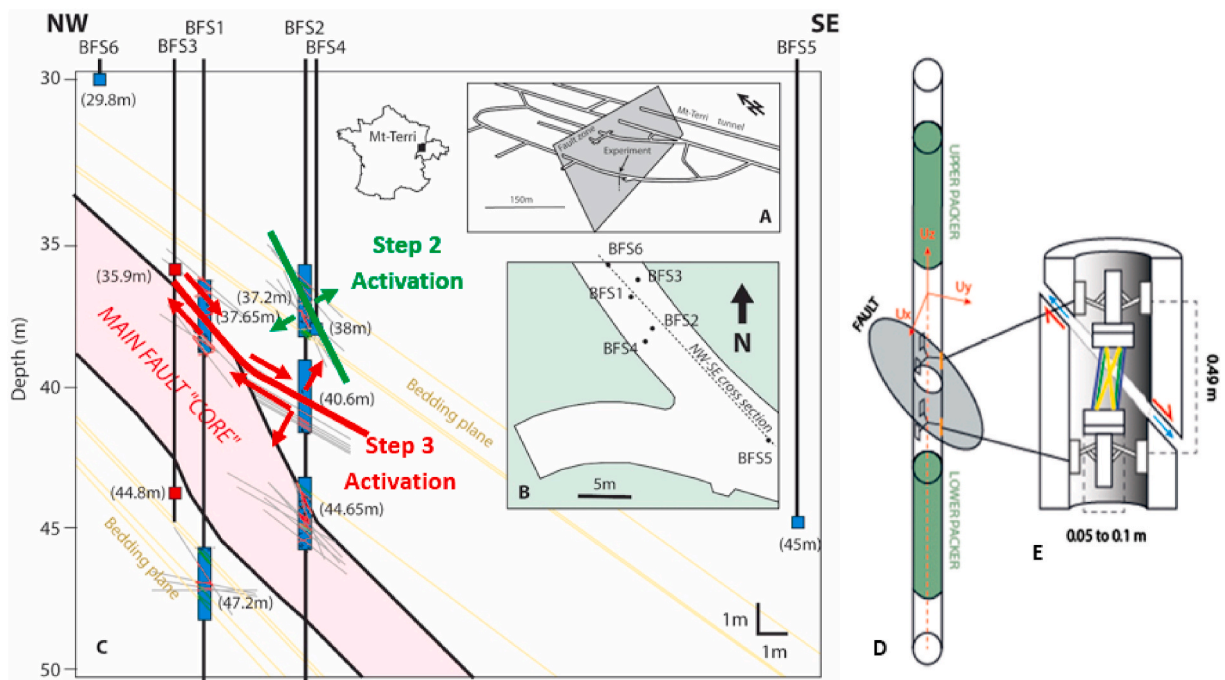
Fig. 2. Fault activation experiments at Mont Terri Laboratory that were used for interpretative modeling in DECOVALEX-2019, Task B. (A) Three-dimensional view of the Main Fault plane with the experimental location; (B) map view of the location of the vertical geologic cross section in (C) and boreholes; (C) Simplified geologic vertical cross section of the Main Fault and boreholes, with blue sections indicating the location of the packed-off sections (test intervals) in boreholes and locations of fault activation experiments modeled in DECOVALEX-2019 marked as Step 2 and Step 3 activations; (D) Isolated borehole injection chamber by upper and lower packers; (E) SIMFIP borehole instrumentation for mechanical deformation measurements across a deforming discontinuity (Modified from Guglielmi et al.[13,15]). (For interpretation of the references to colour in this figure legend, the reader is referred to the Web version of this article.)

approaches and computer codes (Table 1). The fault activation models can be categorized into models representing a fault by an interface and models representing a fault by finite thickness solid elements. In all models, the fault geometry is simplified as a plane cutting the entire model. The differences between interface and solid element representations of faults are conceptually described in Fig. 3. That is, a fracture or fault represented by an interface or discontinuity explicitly models normal and shear displacements as a function of changes in effective normal and shear stress.[13,19–24] Transmissivity for fracture flow can be directly related to fracture aperture through the parallel plate flow assumption.[25,26] For a finite thickness solid element representation of a fracture or fault, a fracture aperture is considered implicitly within the element thickness and equivalent properties are calculated to represent fracture stiffness and flow transmissivity.[27–32] This includes equivalent

elastic modulus and permeability, both of which may involve anisotropy through constitutive models. Another variant is the linking of mechanical codes representing fractures or faults with interface elements to porous media flow in finite thickness elements.[33,34]

A diverse set of numerical simulators (or computer codes) where applied in this study (Table 1). The TOUGH-FLAC simulator[35,36] used by KIGAM and LBNL is based on sequential coupling of the TOUGH2 multiphase flow simulator[37] with the FLAC3D geomechanical simulator.[38] TOUGH-FLAC has previously been extensively applied for modeling fault activation associated with carbon sequestration,[39,40] stimulation of shale gas, and geothermal reservoirs,[41,42] and during production from hydrocarbon reservoirs.[43] For the finite thickness fault element approach, an anisotropic elasto-plastic model is used such that shear failure occurs along the fault plane, considering normal and shear stress across the fault. This is based on the so-called ubiquitous joint model available as a constitutive relationship in FLAC3D, considering failure along weak planes.[38] KIGAM applied both finite thickness elements and interface elements to represent the fault mechanical behavior in TOUGH-FLAC. In the case of interface elements, KIGAM developed new coupling routines between TOUGH2 and FLAC3D through fracture mesh aperture changes calculated in FLAC3D.[22]

OpenGeoSys (OGS) is an open source finite element simulator[44,45] that was applied by the BGR/UFZ and ENSI research teams, respectively using interface and solid element fault models. BGR/UFZ extended OGS towards the capability of dealing with discrete approaches for the simulation of hydraulic fracturing and fault activation. To this end, lower-dimensional interface (LIE) elements with local enrichments have been implemented in OGS.[23,46] The ENSI research team developed and implemented into OGS an elasto-plastic constitutive model that includes sliding failure along weak planes.[32]

Two modeling teams, INER and LBNL, developed models for the fault activation simulations using 3DEC, a code that is based on the Distinct Element Method (DEM). 3DEC handles coupled fluid flow and geomechanics by considering fractures or faults represented by interfaces

Table 1
Modeling team information.

Research Team	Computer Code	Fault Model	Principal investigator(s)	Funding Organization (Country)
BGR/UFZ	OpenGeoSys6	Interface	G. Ziefle J. Maßmann	BGR (Germany)
CNSC	COMSOL	Solid Elements	S. Nguyen	CNSC(Canada)
ENSI	OpenGeoSys5	Solid Elements	L. Urpi B. Graupner	ENSI (Switzerland)
DynaFrax	PFC3D	Interface	J.-S. Yoon	SSM (Sweden)
INER	3DEC	Interface	W. Shiu	Taipower (Taiwan)
KIGAM	TOUGH-FLAC	Interface	J.W. Park	KAERI (South Korea)
	TOUGH-FLAC	Solid Elements	T. Kim	
LBNL	3DEC	Interface	Y. Guglielmi	DOE (USA)
	TOUGH-FLAC	Solid Elements	J. Rutqvist	

1. INTERFACE

- Effective normal stress and shear stress
- Shear and tensile failure
- Shear slip and normal displacement
- Aperture change
- Cubic law fluid flow
- Fluid storage within aperture

2. SOLID ELEMENTS

- Effective normal stress and shear stress
- Shear failure and Plasticity along fault
- Shear and normal strain
- Equivalent permeability
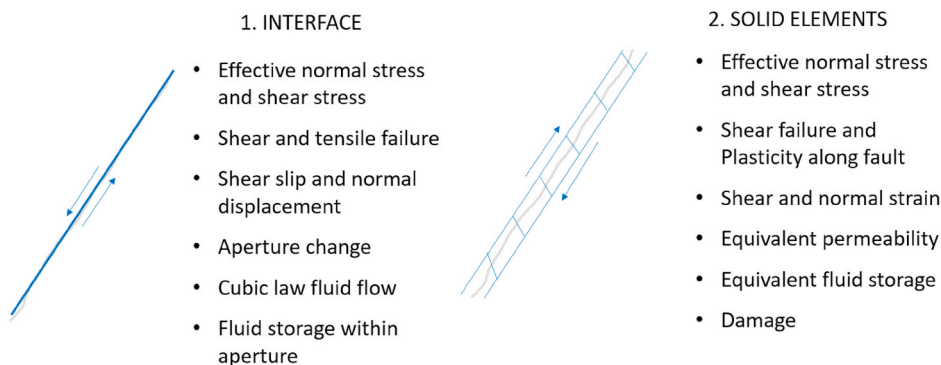- Equivalent fluid storage
- Damage

Fig. 3. Conceptual models and main features for representing faults with interface elements and solid finite thickness elements.

between deformable blocks.[47,48] Finally, the DynaFrax team applied a three-dimensional (3D) particle flow code (namely, Particle Flow Code 3D, PFC3D) to model fault activation.[49] This is also based on DEM, with faults formed between particles through variable bond strength and porous media fluid flow.[50] DynaFrax researchers have in this task extended their particle-flow fault activation modeling to full 3D from previous work in 2D.[51]

In all of the above models, whether finite thickness solid elements or interfaces, a Coulomb criterion was used to evaluate shear failure.[52] As an exception, CNSC considered shear failure using a Drucker-Prager yield criterion.[31] CNSC calculated permeability evolution based on the elastic and plastic strain normal to the finite thickness fracture plane model, including a damage enhancement factor to enhance the effect of plastic normal strain on fracture permeability.[31] This fault activation model was implemented in COMSOL Multiphysics[53] for fully coupled hydromechanical modeling.

4. Step 1 - model inception and benchmarking

A set of well-defined benchmark calculations was first defined to allow for necessary model developments and testing related to fault activation modeling.[17] As opposed to Steps 2 and 3, here the modeling problem is exactly specified, from the model geometry to the rock properties and constitutive relationships such as the fault permeability as a function of aperture and shear. In contrast, in Steps 2 and 3, modeling teams were expected to move from simple benchmarking to complex conceptual model building and comparison of model results with the field experiments.

In the benchmark, the model geometry was defined to broadly

represent the geometry and stress conditions for the subsequent Step 2 fault activation experiment. A 3D model domain was defined to have side-lengths of 20 m and to contain a discontinuity dipping at 65° (Fig. 4). The initial fluid pressure is set to 0.5 MPa, as estimated from site-specific measurements in the Mont Terri Laboratory. The stress field, somewhat simplified from current site-specific estimates[54], assumes that the maximum compressive principal stress is exactly vertical at a magnitude of 7.0 MPa, whereas the intermediate principal stress (and maximum horizontal stress) is oriented exactly normal to the strike of the fault at a magnitude of 6.0 MPa. The minimum horizontal stress is parallel to the strike of the fault at a magnitude of 3.3 MPa, but because it is parallel to the fault this stress does not impact the potential for fault activation. For simplicity, the pressure and stress fields are assumed to be uniform over the 20 m cube domain, neglecting gravity. The outer boundaries of the 20 m cube model are defined to be held at constant fluid pressure of 0.5 MPa and mechanically the displacements normal to each boundary are fixed to zero (roller boundaries). The benchmark injection is conducted in controlled pressure steps as shown in Fig. 5. This injection schedule is the same as was applied in the field during the Step 2 fault activation experiment. A number of monitoring points and profiles were defined for comparison of simulation results between the different teams.[17] Here we focus comparison on injection rate, deformation at the injection borehole and pore pressure at monitoring point P2 located within the fault plane at 1.5 m radius from the injection point (Fig. 4). Borehole deformations where evaluated from relative anchor displacements corresponding to Fig. 2e and with coordinates of anchors defined in Fig. 4b.

The benchmark host rock properties are listed in Table 2. These properties are representative of the Mont Terri Laboratory, but
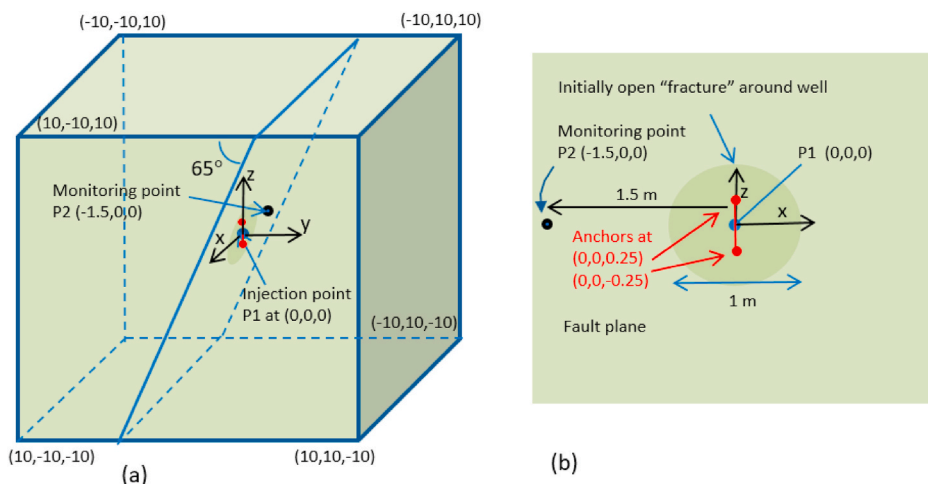

Fig. 4. Model setup for the Step 1 benchmark simulations. (a) 3D model geometry and locations of output points. (b) Detailed view of the fault plane near the injection point.
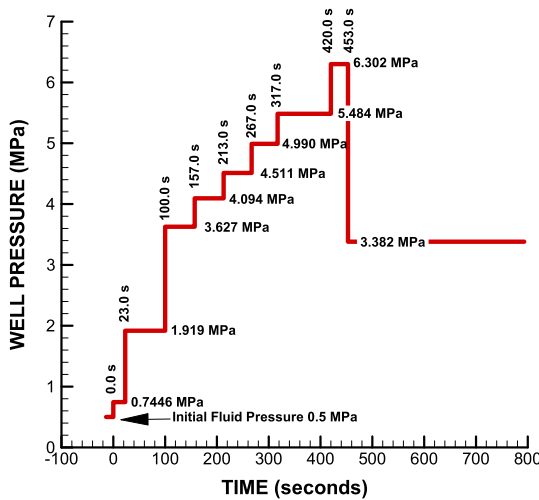
Fig. 5. Injection pressure steps applied at the injection point (P1) in the Step 1 benchmark simulations.

Table 2
Material properties for Step 1 benchmark simulations.

Material	Parameter	Value	
		FM 1	FM 2
Fault (Elasto-plastic)	Normal stiffness, k_n (GPa/m)	20	20
	Shear stiffness, k_s (GPa/m)	20	20
	Cohesion (MPa)	0	0
	Static Friction Angle (°)	22	22
	Dilation angle (°)	0	10
	Tensile strength	0	0
	Initial aperture (μm)	0	10
	Initial creation aperture (μm)	28	0
Host Rock Matrix (Elastic)	Bulk Modulus, K (GPa)	5.9	5.9
	Shear Modulus, G (GPa)	2.3	2.3
	Bulk density, ρ_R (kg/m³)	2450	2450
	Permeability	0	0
Fluid	Density (kg/m³)	1000	1000
	Compressibility (Pa⁻¹)	4.4e-10	4.4e-10
	Dynamic Viscosity (Pa s)	1.0e-3	1.0e-3

simplified in the sense that isotropic and homogeneous properties are assumed over the model domain except for the fault discontinuity. For example, mechanical properties are assumed to be linear elastic and isotropic with a bulk modulus of 5.9 GPa and a shear modulus of 2.3 GPa, which represent average values at the Mont Terri Laboratory.[54,55] Moreover, the host rock is considered impermeable, which is reasonable considering the very low permeability of undisturbed Opalinus Clay and the relative short duration of these experiments.

In these benchmark simulations, a single fault or fracture plane is defined with opening as a result of changes in effective stress assuming a linear elastic normal stiffness, but with a tensile strength of 0 MPa. That is, effective normal stress is governed by (assuming compressive stress is positive)

$$\sigma'_n = \sigma_n - P, \tag{1}$$

where σ'_n and σ_n are effective and total normal stresses [Pa], respectively, and P is fluid pressure [Pa].

Shear displacement is assumed to be governed by a linear elastic shear stiffness and a shear strength according to the Coulomb criterion. Based on site investigations at Mont Terri and some initial test simulations, the friction angle was set to 22° with a cohesion equal to 0.

Fluid flow along the fault is governed by Darcy's law with cubic dependency between flow rate and hydraulic conducting aperture, i.e. the fluid flow per unit width is calculated as

$$q = -\frac{b_h^3 \rho g}{12\mu} \nabla h \tag{2}$$

where b_h is hydraulic conducting aperture [m], ρ is fluid density [kg/m³], g is the acceleration due to gravity [m/s²], h is hydraulic head [m], μ is dynamic fluid viscosity [Pa s], and ∇ is the gradient operator. For simplicity, it is assumed that the hydraulic conducting aperture is equal to a mechanical aperture with the change in fracture aperture being equal to fracture normal displacement.

The hydraulic aperture is comprised of an initial aperture [m], b_{hi}, an induced fracture creation aperture [m], Δb_{hc}, an induced elastic aperture change [m], Δb_{he}, and an induced aperture change due to shear dilation [m], Δb_{hs}, according to:

$$b_h = b_{hi} + \Delta b_{hc} + \Delta b_{he} + \Delta b_{hs}. \tag{3}$$

Two different models or parameter sets are applied for dealing with shear-induced hydraulic aperture changes, and associated changes in fracture transmissivity.

FM1: An elastic (normal) and plastic (shear) opening of the fault is only possible when shear failure occurs.

FM2: An already existing aperture of the fracture, where elastic (normal) opening is allowed from the beginning with propagating pore pressure, while shear (dilatant) opening is only possible when shear failure occurs.

FM1 (Fault Model 1) is defined based on experience with modeling similar fault activation experiments at the Tournemire site in Southern France.[56] It is a simple model, but one that reasonably reproduced measured responses at the Tournemire site. In this model, as soon as shear- or tensile-failure occur, an induced change in aperture of $\Delta b_{hc} = 28$ μm occurs, signifying that an open fault surface has been created. The value of $\Delta b_{hc} = 28$ μm comes from the modeling and evaluation of similar field experiments at the Tournemire site.[56] Thereafter, the fracture can respond as a function of effective normal stress [Pa], σ_n, depending on the fracture normal stiffness [Pa/m], k_n, according to:

$$\Delta b_{he} = \Delta \sigma'_n / k_n. \tag{4}$$

The relations used in FM1 were applied by Guglielmi et al.[56] at the Tournemire site because measurements indicated substantial permeability increases with shear displacement despite an apparent lack of shear dilation.

The second fault model (FM2) could be viewed as a more conventional hydromechanical fracture model in which hydraulic aperture is equal to the mechanical aperture that in turn depends on opening as a result of reduction in effective stress, fracturing, and shear dilation governed by

$$\Delta b_{hs} = u_s \times \tan \varphi, \tag{5}$$

where u_s is shear displacement [m] and ϕ is the dilation angle [°], which in FM2 is set to 10°.

The model parameters for FM1 and FM2 are listed in Table 2. These parameter values have been developed from the site investigations at the Mont Terri Laboratory, including laboratory and field testing.[54,55] Therefore, the parameters listed in Table 2 were used as a starting point for the subsequent Step 2 and Step 3 modeling.

Fig. 4b shows a view of the fault plane for FM1. The figure shows that an initial fracture exists around the well to a radius of 0.5 m which has an aperture equal to the creation aperture of 28 μm. In the case of FM2, a uniform initial aperture of 10 μm exists in the entire fault plane from the injection point to the outer boundaries. The 28 μm creation aperture is taken from Guglielmi et al.,[56] whereas the 10 μm initial aperture is arbitrarily defined as a small initial aperture for the benchmark calculations. These differences in the fault hydromechanical models cause strongly different hydromechanical behavior between FM1 and FM2.

Each of the modeling teams listed in Table 1 used their respective

numerical simulators to build the models according to the benchmark description. For comparison of the modeling results between the teams, a number of monitoring points and profiles were defined. These included the injection flow rate, as well as the pressure at the injection point (P1) and the monitoring point (P2) located 1.5 m from the injection. Moreover, the relative displacements between two points bracing the fault vertically at the injection point were compared corresponding to a SIMFIP measurement (Figs. 2e and 4b). Such output results and comparison between the modeling teams are shown in Figs. 6 and 7 for FM1 and FM2, respectively.

In the case of FM1, an abrupt increase in the injection flow rate (Fig. 6a) and pressure at the monitoring point P2 (Fig. 6b) occurs after about 420 s. This is followed by an abrupt decrease after around 450 s. These abrupt flow and pressure responses are a result of the fault hydromechanical model assumed for FM1. Before 420 s, the initial 0.5 m radius fracture is pressurized step-wise which causes elastic fracture opening locally, as observed in the calculated anchor displacements (Fig. 6c) and normal displacements (Fig. 6d). At about 420 s, the pressure is sufficiently high to cause the rupture to propagate from the initial 0.5 m radius to and past the monitoring point P2 located at a radius of 1.5 m. Along with this rupture propagation, shear failure and shear slip occur, as was calculated by most models (Fig. 6d). At 450 s, the injection

pressure is stepped down, the fracture closes, and the injection flow rate decreases to a small value.

In the case of FM2, the hydromechanical response of the fault follows the step-wise increase and subsequent decrease of the injection pressure (Fig. 7). This behavior reflects the FM2 fault hydromechanical model where a fracture with an initial aperture of 10 μm exists that connects the injection point at P1 with the monitoring point at P2. Thus, the injection flow rate (Fig. 7a) increases with each injection pressure step at P1 as a result of increasing pressure gradient and permeability caused by fracture opening, and a pressure increase at P2 is recorded almost immediately after each increase at P1. At the peak injection pressure of 6.3 MPa, shear failure occurs with some calculated shear slip for most models (Fig. 7d).

Overall, the different models applied to this benchmark show a general agreement in the modeling results regarding the activation mechanisms and trends, though some discrepancies occur, especially for FM1. In the case of FM1, the agreement is very good during the first 420 s, when pressurization of the existing fracture around the injection point results in elastic opening. The timing of the rupture and flow increase is also in good agreement. However, the extent of rupture propagation, the magnitude of shear slip, and the total injection volume differ significantly for some models. Two teams, BGR and KIGAM, did not achieve
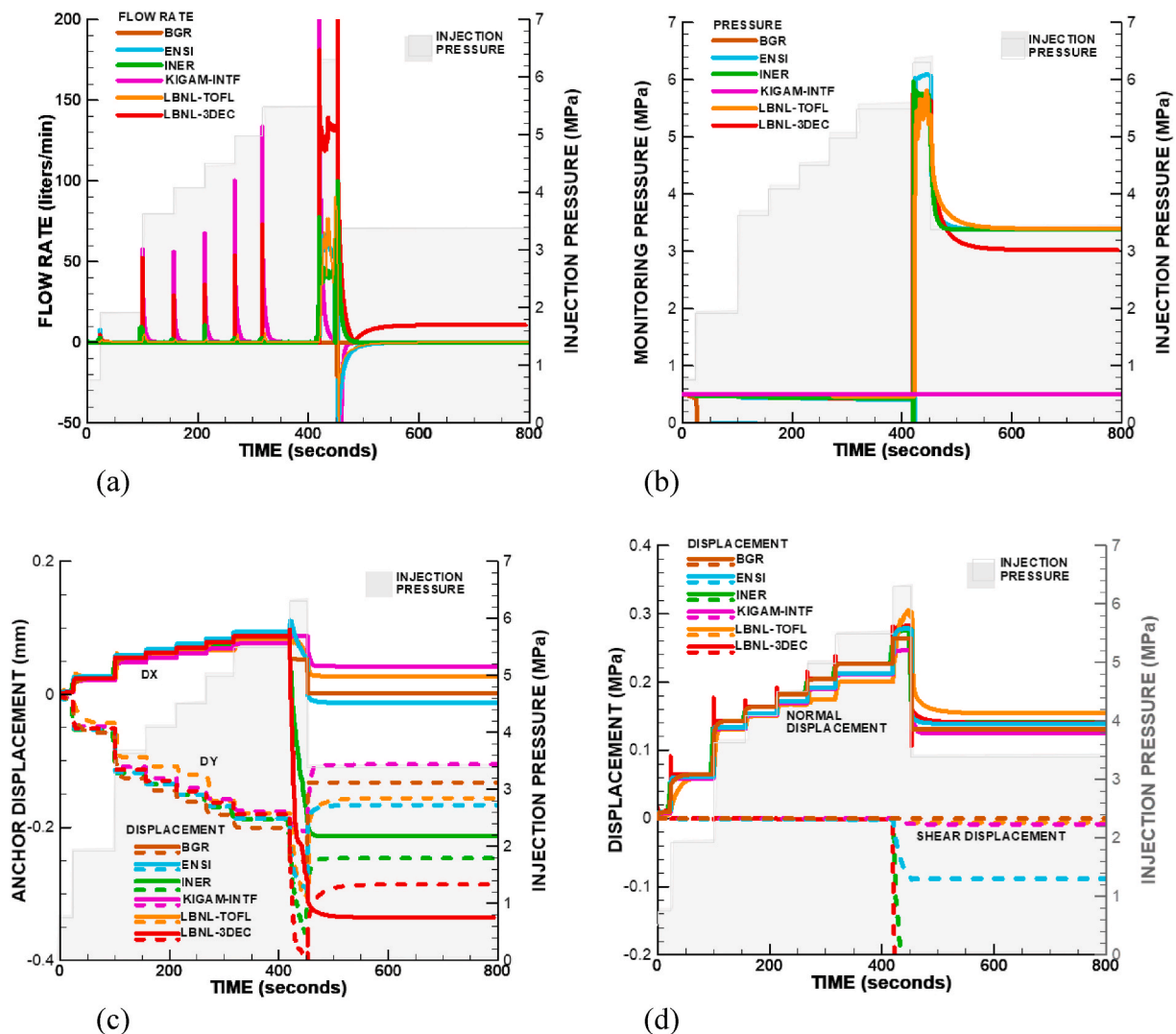

Fig. 6. Modeling results for the FM1 benchmark with input injection pressure at P1 in gray shade. (a) Injection flow rate, (b) pressure at P2, (c) anchor displacements at P1, and fracture normal and shear displacements at P1. (For interpretation of the references to colour in this figure legend, the reader is referred to the Web version of this article.)
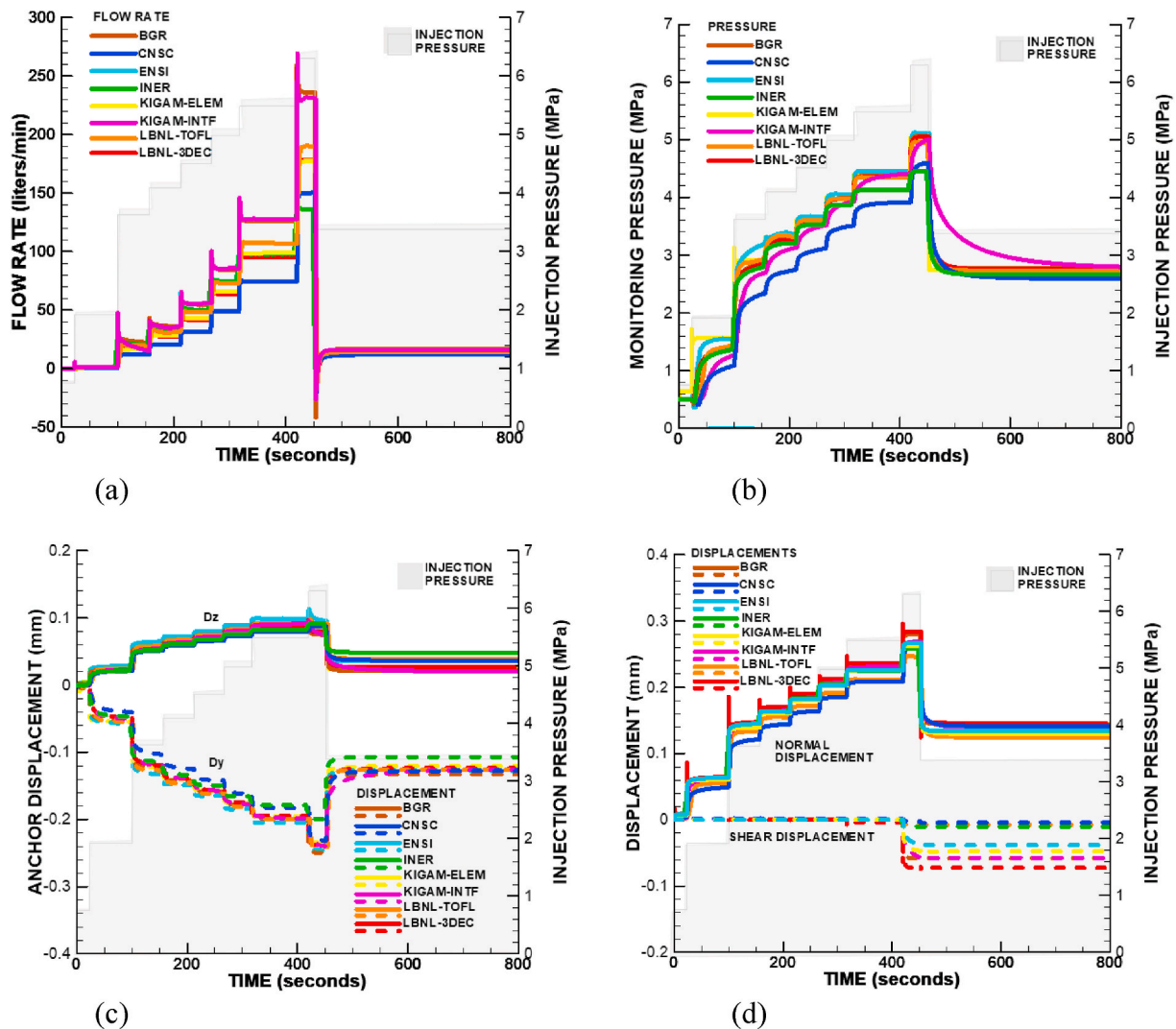
Fig. 7. Modeling results for the FM2 benchmark with input injection pressure at P1 in gray shade. (a) Injection flow rate, (b) pressure at P2, (c) anchor displacements at P1, and fracture normal and shear displacements at P1. (For interpretation of the references to colour in this figure legend, the reader is referred to the Web version of this article.)

rupture propagation all the way to P2 and consequently no pressure increases occurred at P2 (Fig. 7b). The two teams that used the DEM code 3DEC calculated much larger shear slip displacements than other teams. Also in the case of FM2, the biggest disagreement between the modeling results occurs for the shear slip magnitude towards the end of the simulation (Fig. 7d). This shows that the greatest model uncertainty will be on the modeling of shear slip, whether slip does occur and if so what it's magnitude will be. Shear failure is a hydromechanical response that can depend on very small differences in shear stress and shear strength on the fault. These evolve over time and are sensitive to modeling choices, such as the mesh discretization or the fault modeling approach, including interface versus finite thickness elements. In FM2, some disagreement also occur in the flow rate response (Fig. 7a), which is affected by the very sensitive cubic-law relationship between flow rate and aperture.

5. Step 2 – modeling activation experiment in the fault damage zone

In the following subsections, we first present the Step 2 field experiment and data with some general observations and interpretations, followed by the models and their parametrizations, and finally the model results with comparison between simulated and experimental data.

5.1. Field experimental data

The Step 2 fault activation experiment was conducted by fluid injection into a 2.4-m long isolated injection chamber of borehole BFS2 with monitoring of fluid pressure responses in borehole BFS4 located at a horizontal distance of 1.5 m (Fig. 2 and 8). Guglielmi et al.[14] describes 12 discontinuity planes intersecting the injection chamber of BFS2 being pressurized during the experiment (Fig. 8). Most of these discontinuities strike N030°-060°E and dip 50–70°SE and thus one or several of these discontinuities could be opened and activated during the borehole pressurization. Also, the monitoring borehole BFS4 is located along the strike of those discontinuities and signals measured there can indicate when flow paths form along one or more of these discontinuities (Fig. 8c). The stress field estimated at the Mont Terri Laboratory[54,57–59] is oriented such that the maximum stress is approximately vertical at a magnitude of 6–7 MPa, while the intermediate principal stress is approximately horizontal at 4–5 MPa and oriented approximately perpendicular to the average strike of the discontinuities observed in the BFS2 borehole section (Fig. 8a and b).

The specific injection cycle analyzed for Step 2 was the first of several injection cycles performed using an electric motor pump. However, this
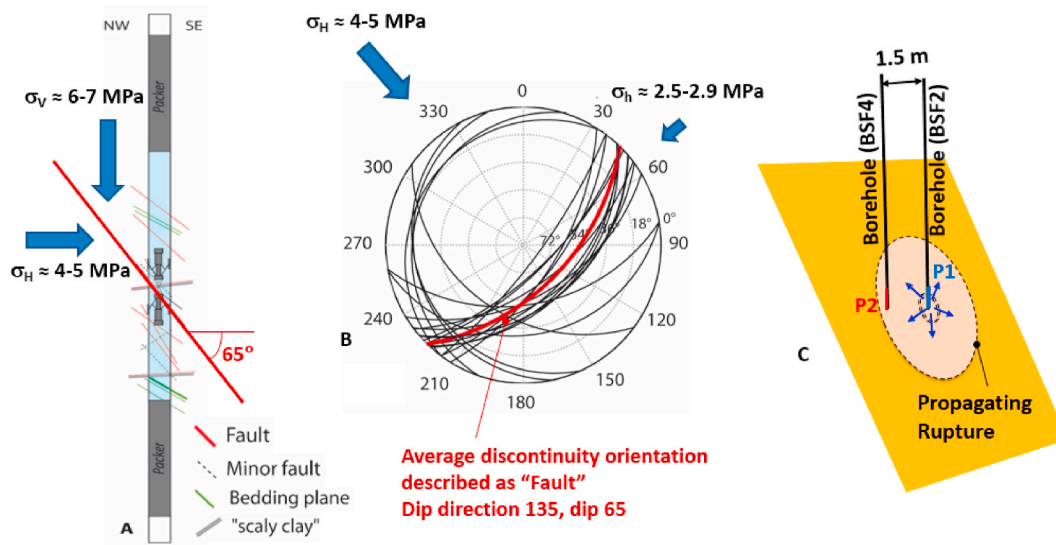
Fig. 8. Mapped fractures within injection chamber of Step 2 fault activation experiment and synthesized Mont Terri stress estimates based on Corkum and Martin[54] and Amann et al.[59] (A) vertical cross section of the injection chamber, (B) lower hemisphere stereographic projection with average discontinuity orientation marked in red, and (C) conceptual model of injection-induced rupture propagation along the weak plane to finally connect P1 with P2. (For interpretation of the references to colour in this figure legend, the reader is referred to the Web version of this article.)

borehole interval had previously been pressurized using a hand pump, which resulted in a fracture created along an intersecting discontinuity plane. This fracture corresponds to the created fracture shown in Fig. 4 for the FM1 benchmark example, which indicates that activation must have been initiated along one of the discontinuities (weakness planes) intersecting the injection interval. The motor pump injection would result in further propagation of this initial fracture to beyond the

monitoring well according to the conceptual model in Fig. 8c.

Fig. 9 presents the field data during this injection experiment in which the injection pressure followed the schedule similar to the one shown in Fig. 5. Injection flowrate, injection chamber pressure and borehole displacements were monitored at a 500 Hz sampling frequency. The borehole deformations were measured between anchors, fixed to the borehole wall in a 0.5 m vertical section of the injection
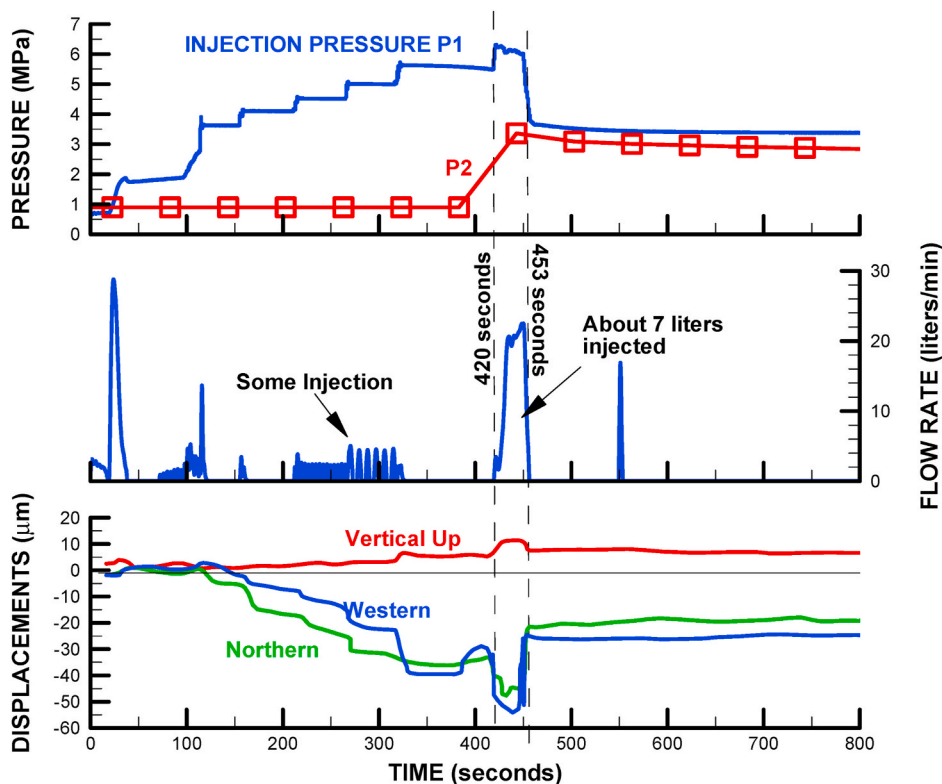

Fig. 9. Field data related to the Step 2 fault activation experiment conducted within the damage zone of the Mont Terri Main Fault (Modified from Guglielmi et al.[13]). (Top) Controlled injection pressure P1 in BFS2 and resulting pressure response P2 at BFS4, (Middle) injection rate into BFS2 and (Bottom) anchor displacements at the injection borehole BFS2.

borehole (Fig. 2). Thus, the deformation measurements are anchored within the central part of the injection chamber. The anchor displacements shown in Fig. 9b are the displacements of the upper anchor relative to the lower anchor, in vertical up, northern and western directions. Moreover, the relative displacements shown in Fig. 9b have been corrected to filter out elastic deformations of the equipment and injection chamber in order to deduce the displacement of the discontinuity itself.[15]

The fluid flow data in Fig. 9 show a sharp increase in injection flow rate at about 430 s, which is about 10 s after the injection pressure was increased to the peak pressure of just above 6 MPa. At this point in time, a sharp increase in fluid pressure can be observed at the monitoring point in borehole BSF4, located about 1.5 m horizontally from the injection point. Thereafter, as the injection pressure is reduced below about 4 MPa, an abrupt decrease in injection flow rate is noted at 453 s. The anchor displacements in Fig. 9 indicate that fracture deformation occurs already during the first few injection pressure steps, with displacements correlated to injection pressure steps. This may be interpreted as opening of the small fracture around the injection borehole that had been previously created during the initial hand pump injection. The displacements shown in Fig. 9 indicate opening of a steeply dipping discontinuity with a strike and dip similar to those shown in Fig. 8. However, these anchor measurements can be a result of complex discontinuity opening and shear that can be analyzed in more detail with coupled hydromechanical numerical modeling.

5.2. Models and parameters

The teams applied similar models to those that had been developed and verified in the previous benchmark tests. Also, most teams assumed a similar geometry, i.e., activation of a discontinuity dipping 65° and with the strike being approximately parallel to the minimum principal stress direction. As seen in Fig. 8, this is consistent with the estimates of the in-situ stress field at Mont Terri.[46] This means that the potential for shear activation of the fault would depend on the shear stress as a result of the difference between the vertical and maximum horizontal stress magnitudes.

Fig. 10 shows the mesh design for the six different models applied by various teams for the Step 2 modeling. CNSC's COMSOL and LBNL's TOUGH-FLAC models are half symmetric, which is possible considering the orientation of the fault relative to the stress field, with the minimum compressive stress oriented along the strike of the fault. Other models, including KIGAM's TOUGH-FLAC model, ENSI's OGS model, as well as LBNL's and INER's 3DEC models include the entire 20 m cube and can therefore be exposed to a stress field that is not exactly orthogonal to the strike of the fault.

All teams, except CNSC, considered a fault hydromechanical model based on FM1. That is, rupture propagation along an initially impermeable weakness plane formed by the discontinuity. As soon as rupture occurs, a fracture creation aperture is added, which results in a substantial increase in the local fracture permeability. The CNSC team used a model that is more similar to FM2, but with the addition of a "damage enhancement permeability factor" associated with plastic strain. This damage enhancement factor correlates with failure and thus may have a similar effect on local fracture permeability as the fracture creation aperture model adopted by other teams.

Table 3 summarizes key parameters of all the six models. As learned from modeling of the previous benchmark experiments, the key for predicting the timing of the rupture is to accurately calibrate the parameters to induce shear failure or tensile failure and rupture propagation at 420 s. All teams applied a friction angle of 22°, which was a parameter given to the teams in the earlier benchmark calculation and this value is based on laboratory testing on Opalinus Clay within the Mont Terri project.[54,55] A number of teams also followed the benchmark calculation by assuming a cohesionless fault, i.e., cohesion was set to 0. Note that this would also imply a tensile strength equal to 0. Considering such strength properties, teams then varied the stress magnitudes and orientations to calibrate for rupture initiation and thereby attempted to achieve the best possible match with observed data.

5.3. Modeling results with comparison to field data

Fig. 11 presents comparison of the field data with the simulation results obtained with the six models that were applied to the Step 2 fault activation experiment. A good agreement with field data is obtained by all the modeling teams regarding the timing of the abrupt flow rate
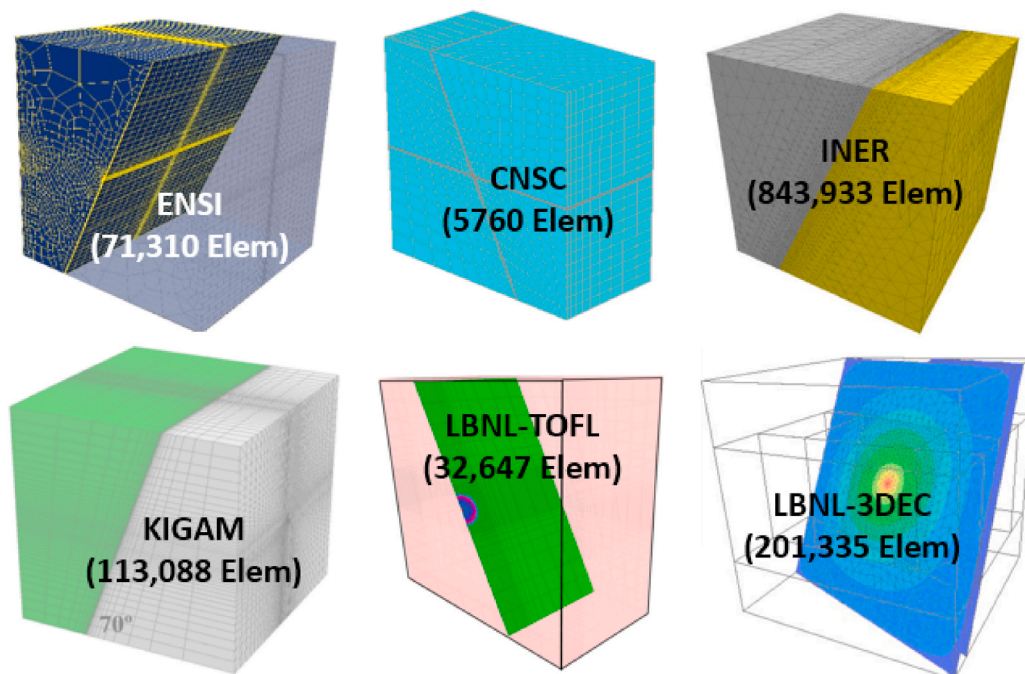

Fig. 10. Mesh discretization applied by the different teams for modeling the Step 2 fault activation experiment.

Table 3

Key parameters applied by the different modeling teams derived from the interpretative modeling of the Step 2 fault activation experiment.

| Input parameters		Unit	ENSI	CNSC	KIGAM	INER	LBNL TOUGH	LBNL 3DEC
Fault	Normal stiffness	GPa/m	120	60	60	60	116	35
	Cohesion	MPa	1.45	0	0.2	0	2.0	0.5
	Friction angle	°	22	22	22	22	22	22
	creation aperture	μm	28	(damage)	40	28	28	10
	Fault Dip direction	°	132	135	140	145	135	135
	Fault Dip	°	80	65	70	82	65	60
Initial stress	σ_v	MPa	6.0	7.0	5.1	5.7	6.0	6.0
	σ_H	MPa	4.2	6.0	5.0	5.8	4.2	5.7
	σ_h	MPa	3.3	3.2	2.0	4.9	3.3	4.5
	σ_H direction	°	132	135	140	150	135	137
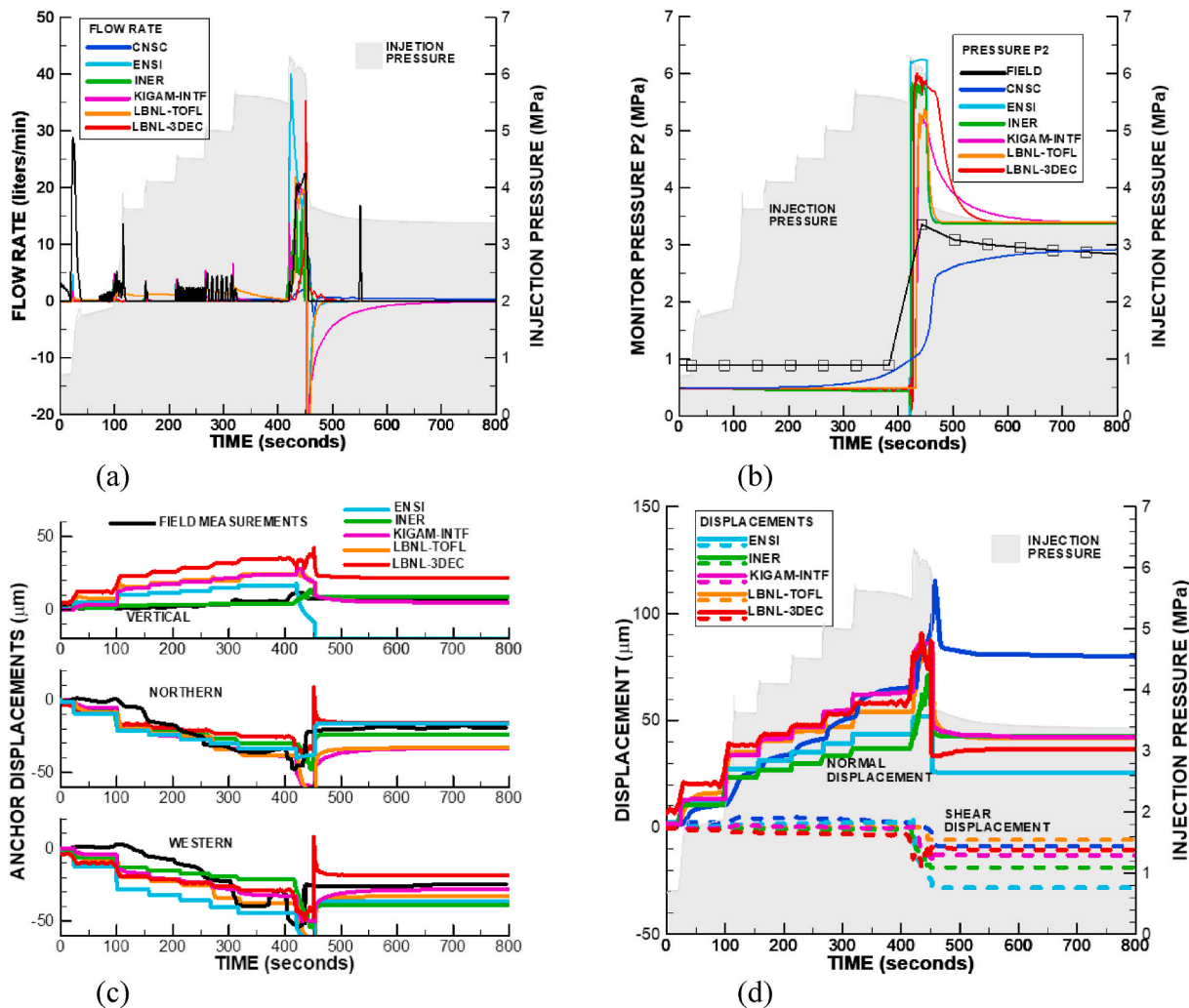
Fig. 11. Comparison of modeling results with field data for the Step 2 fault activation experiment with the controlled injection pressure in gray shade and other field data in black. (a) Injection flow rate, (b) pressure at P2, (c) anchor displacements at P1, and (d) fracture normal and shear displacement at P1. (For interpretation of the references to colour in this figure legend, the reader is referred to the Web version of this article.)

increase at 430 s and the subsequent flow rate decrease at 453 s (Fig. 11a). A similarly good agreement is achieved for the timing of the pressure response at the monitoring well (Fig. 11b), as well as the trends of the borehole anchor displacements (Fig. 11c). Some systematic difference can be observed between the teams that used the FM1 approach with rupture propagation along an impermeable weakness plane compared to CNSC who was using the FM2 approach with reopening of an initially slightly permeable discontinuity. The CNSC modeling shows a smoother pressure response at the monitoring borehole with a final pressure at the end (800 s) that is closer to the field measurements.

The total injection flow volume and the evolution of the injection rate is captured very well by most teams (Fig. 11a). The key parameters for matching the measured peak flow rate are the creation aperture (or damage enhancement factor) and fracture normal stiffness. These parameters determine how much permeability and flow rate can increase as a result of rupture and subsequent changes in effective normal stress as fluid pressure propagates into the created fracture. CNSC who uses an FM2 model, substantially underestimates the peak flow rate and total injection volume. Further sensitivity studies would be required to determine the exact reason for the lower injection rate achieved by

CNSC, though it could be a matter of the choice of damage-permeability factor. Finally, there is an apparent disagreement between model results and experiments related to flow back. As observed in Fig. 11a, the modeling resulted in a significant flow-back volume seen as a negative flow rate after 453 s. In the experiments, fluid was released by opening a valve and letting the fluid flow back to reduce the injection borehole pressure, but the rate of flow back was not measured. Thus, we have no means of comparing modeled and experimental flow-back volumes.

Good agreement is achieved regarding the relative anchor displacements, especially for the north and west relative displacements (Fig. 11c). The north and west displacements are each at an angle approximately $+45°$ and $-45°$ off the discontinuity dip direction, but are approximately equal in magnitude. This fact, together with the somewhat smaller magnitude of the vertical relative anchor displacements, indicates a fracture opening rather than shear as the dominant mechanism. The key parameters to match the measured anchor displacements are normal stiffness, shear stress, shear strength, and the dip of the discontinuity. The normal displacement determines the fracture opening that occurs at each pressure step during the initial 420 s of the injection. Thereafter, around 420 s, the rupture occurs, which induces some additional displacements and this is followed by a rebound when the injection pressure is reduced.

While the modeling results are in very good agreement with the two horizontal displacements (northern and western), the vertical displacement is generally overestimated. The teams that are closest to match the vertical displacement are INER and ENSI who are using a fault dip of 82° or 80°, respectively, rather than 60–70° used by other teams. In fact, the initial elastic opening was used by INER to determine the exact orientation of the opening discontinuity. The INER team noted a slightly larger initial elastic displacement in the northern compared to the western direction and therefore set the dip direction of the discontinuity to N145 rather than N135 that was used by most other teams. However, the steep fault dip of 80 or 82° is steeper than any detected discontinuity on the borehole wall.

After reaching the peak injection pressure of 6 MPa, most teams calculated a shear failure with a relatively small shear displacement (Fig. 11d). For most teams, such shear displacement impacted the vertical displacement, leading to a rebound that is most obvious in the results for ENSI, who obtained the largest dip-slip shear displacement. Several modeling teams found that a large shear slip upon shear failure

needs to be prevented in order to match the observed anchor displacements. This was achieved by some of the teams by either keeping the shear stress on the fault relatively small (i.e., limiting the difference between σ_V and σ_H), or by considering an increased cohesion. INER and LBNL-3DEC used a horizontal principal stress field not exactly parallel and normal to the strike of the discontinuity to capture an observed dominant (though small) strike-slip shear displacement.

6. Step 3 – modeling fault activation experiment at the fault core

For the Step 3 fault activation experiment, we first present the field experiment and data with general observations and interpretations, followed by the models, their parametrization, and results for the two modeling teams who completed the Step 3 fault activation modeling.

6.1. Field test data

The Step 3 fault activation experiment was conducted by injecting into another interval of BFS2 closer to the core of the Main Fault (Figs. 2 and 12). During this injection experiment, fluid pressure and deformation were monitored at the injection borehole BFS2 and at the monitoring borehole BFS1 (about 3.5 m away in horizontal direction), at an interval which straddles the upper boundary of the fault core. The Step 3 fault activation experiment is more complex than Step 2, involving opening and shear deformations first along a discontinuity in the damage zone of the Main Fault which then connects with a prominent discontinuity along the interface between the fault core and the adjacent fault damage zone.[14]

Fig. 12 presents a detailed view of the injection interval, which is located in the fractured damage zone, about 3.4 m above the fault core interface. As determined by a borehole optical log, the injection chamber is intersected by 13 subparallel fault planes with a strike of N40-50 E and a dip of 35-55SE (Fig. 12c). As noted in Guglielmi et al.,[13] the displacement sensor is anchored across a 2-to-3-cm-thick minor fault that is striking N42E with a dip of 36SE. In the monitoring hole, the displacement sensor is centered at 35.9 m depth (measured from the overlying tunnel) across the upper boundary of the fault core, which is locally oriented N50°E and dipping 61°SE (Fig. 2).

Fig. 13 shows experimental data of injection flow rate and pressure at BFS2, as well as pressure and displacements at BFS1. An abrupt increase
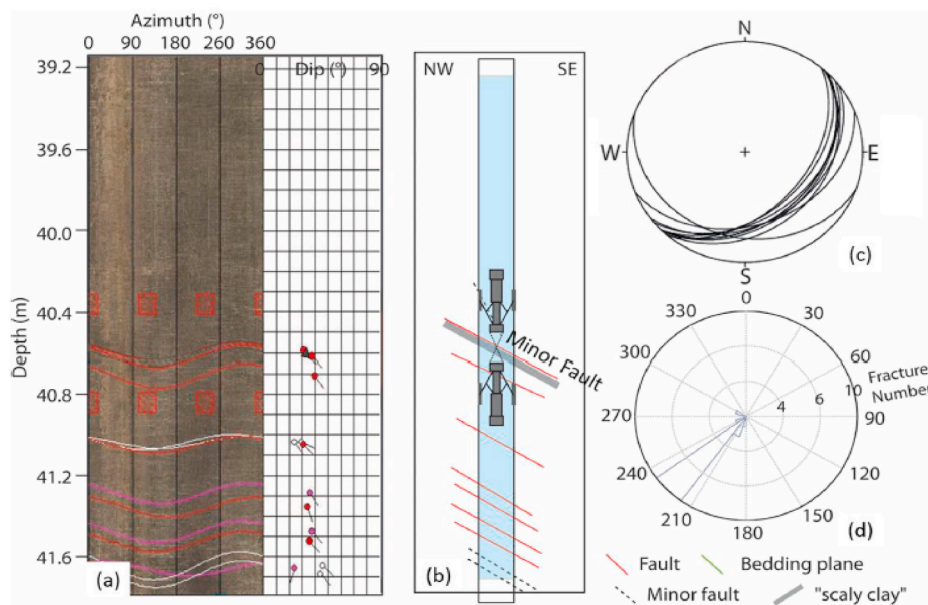

Fig. 12. (a) Optical log of the injection interval. (b) Schematic geological structure of the interval with the displacement sensor's location. (c) Stereographic lower hemisphere plot of the interval fractures. Rose diagram of the interval fractures orientations.[15]
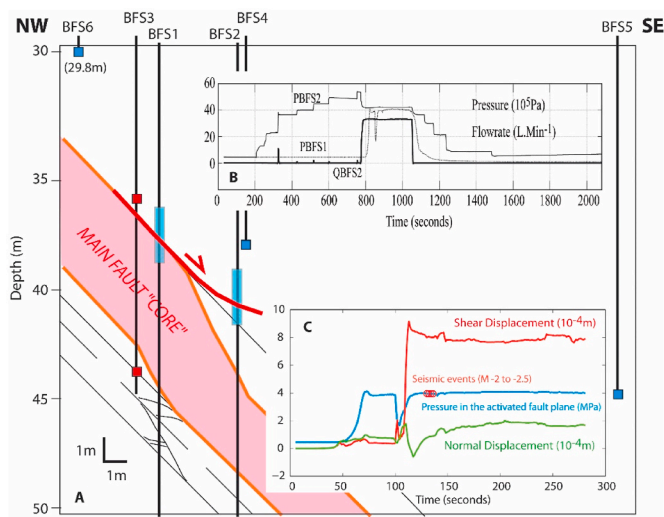
Fig. 13. Cross-section view of the activated fault patch, B – Pressure and flowrate-vs-time variations at the injection chamber (respectively PBFS1 and QBFS1 continuous lines) and pressure-vs-time variations at the monitoring chamber (PBFS2 dashed line), C – Detail of pressure-shear-normal- seismic displacements-versus-time measured on the Main Fault in the BFS1 monitoring chamber (red circles figure when events triggered during the test) (Modified from Guglielmi et al.[14,15]). (For interpretation of the references to colour in this figure legend, the reader is referred to the Web version of this article.)

in flow rate occurs in the injection chamber of BFS2 once the pressure increases to between 5.4 and 5.7 MPa. A hydraulic connection establishes quickly between the injection (BFS2) and the monitoring chamber (BFS1), about 21 s after the rupture occurs at the injection hole. At this instance, a pressure increase of up to 4.2 MPa is observed in the monitoring borehole at the fault core, about 3 m away from the injection hole.

Fig. 13C shows a temporal close up of the pressure evolution, as well as the shear and normal displacements evaluated from the borehole deformation tool in the monitoring chamber BFS1. Included is also the occurrence of a swarm of small micro-seismic events. A millimeter sized shear displacement is triggered, which is partly aseismic since seismic events were only recorded *after* the main shear. These displacements are about 2.4 times larger than in the injection fault segment, corresponding to a normal fault activation. In detail, hydromechanical coupling effects are very complex, potentially occurring on several different fault planes affecting the BFS1 interval. For example, a large pressure drop is observed at the onset of the main shear displacement in BFS1, but not in BFS2, indicating a hydraulic de-connection between the injection and the monitoring points. Following this pressure drop, an apparent closing of the fault while shearing is observed.

6.2. Models and parameters

It was found early on that a successful simulation of the Step 3 fault activation experiment requires to include at least two intersecting discontinuities: one representing the fracture or minor fault connecting the injection well to the fault core, and another discontinuity representing the interface between the fault core and the surrounding damage zone. Four modeling teams, LBNL, ENSI, CNCS and DynaFrax attempted to model this experiment and provided some results for comparison.[17] The LBNL, ENSI and CNSC applied the same conceptual relationships for hydromechanical coupling as used and validated against the Step 2 experiment, whereas DynaFrax applied a newly developed three-dimensional fault hydromechanical model using the PFC3D code. Here we present comparison for two teams, LBNL and ENSI, that managed to model and provide a complete set of results for comparison of hydraulic and mechanical responses at both the injection and monitoring wells.

Fig. 14 shows the models of LBNL-3DEC and ENSI, containing the two main discontinuities, with an additional discontinuity added in the LBNL-3DEC model. This additional discontinuity belongs to a discontinuity set observed mainly in the fault zone while not common in the injection interval. The discontinuity intersecting the injection interval in BFS2 is described in Guglielmi et al.[15] as a minor fault consisting of a discontinuity plane and a centimeter thick layer of shaly scale (Fig. 12). This minor fault intersects BFS2 with a dip of 36° to the SE at a strike of N42E, which is approximately parallel to the minimum compressive horizontal stress (σ_h). In both LBNL-3DEC and ENSI models, this discontinuity is assumed to strike parallel to σ_h, while the dip is set to 37° in the LBNL-3DEC model and 30° in the ENSI model. The discontinuity at the boundary of the fault core has a dip of 60° to the SE in both the LBNL-3DEC and ENSI models. However, the strike has been somewhat simplified in the ENSI model to be exactly parallel with the minor fault in BFS2 and hence parallel to σ_h.

Table 4 lists the key parameters used by the ENSI and LBNL teams to model Step 3. Both LBNL and ENSI used an approach based on the FM1 concept, similar to what these teams applied in the Step 2 experiment. The Step 2 parameters were used as a starting point, but then fine-tuned to match the Step 3 experimental data in terms of timing and magnitudes of flow rate, pressure and borehole deformations. The final set of parameters are very consistent between the two teams (Table 4). These include an equivalent stress field, with exactly the same values of σ_V = 5.5 MPa and σ_H = 4.7 MPa, as well as the same friction angle and creation aperture, whereas there are some small differences regarding fracture normal stiffness and cohesion. The cohesion is higher in the case of ENSI (0.85 vs 0.5 MPa), which may be a result of a different dip of the minor injection fault (30 vs 37°). The main difference is the model architecture with the additional discontinuity in the LBNL model, which also very much favorably oriented for slip.

6.3. Modeling results with comparison to field data

Fig. 15 presents selected results from the ENSI and LBNL-3DEC simulations with comparison to the field measurements. The simulation for LBNL-3DEC was stopped after about 900 s as the fluid pressure had propagated toward the outer boundary and was thereafter impacted by boundary effects.[15] The simulation results are in reasonable agreement with measured data, in particular the timing of the sudden increases and decreases of the flow rate, which occur after 800 and 1050 s, respectively. The simulated evolution of pore pressure in the BFS1 monitoring chamber also agrees well with the measurements with respect to timing and pressure magnitude. The simulations show that a high permeability connection has formed along the two connected discontinuities and is held open at a pressure of about 4 MPa. Water is injected at a high rate until the injection is shutdown at about 1050 s when the injection pressure is reduced below 4 MPa. Whereas both LBNL and ENSI accurately capture the timing of the injection rate, ENSI's modeling results show only about one third of the measured injection rate. In contrast, LBNL's results agree well with the observed injection rate.

For Step 3, the field data include relative anchor displacements at both the injection and monitoring boreholes, via two SIMFIP probes installed at these locations. Here we compare simulation results with the relative anchor displacements at the monitoring point in BFS1, at the fault core boundary (Fig. 15c). LBNL's results display larger magnitudes than ENSI results although both models reproduce well the orientation of the displacements. At 800 s, LBNL displacements show a sharp displacement variation followed by a partial more progressive reverse effect. This is in good agreement with what is observed in the measurements at 820 s (the model rupturing 20 s before what is observed in the field). This is not reproduced in the ENSI model results for the reason that it corresponds to the activation of the additional discontinuity which is only included in the LBNL model.

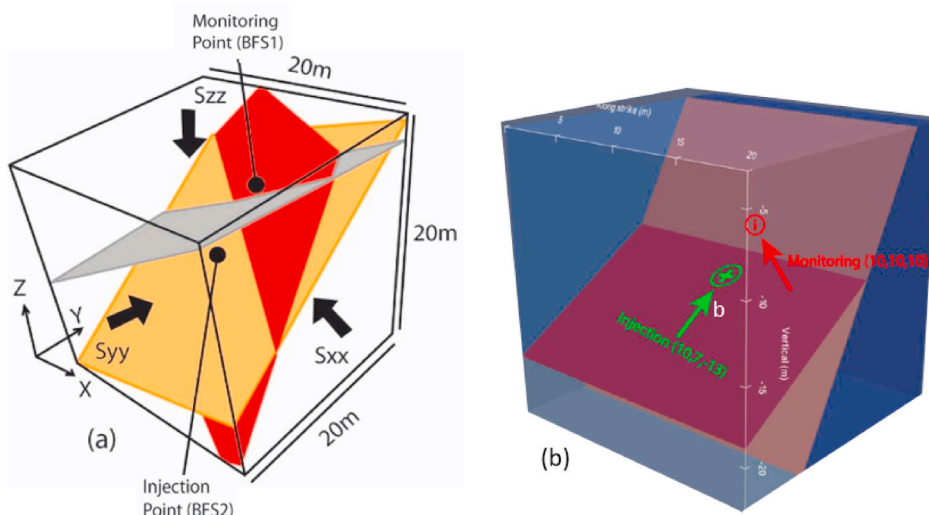Fig. 15d shows the displacements in Fig. 12c re-plotted but here in

Fig. 14. Model geometry for modeling Step 3 fault activation experiment. (a) LBNL model for 3DEC, and (b) ENSI model for OGS (modified from Guglielmi et al.[15] and Urpi et al.,[32]).

Table 4
Key parameters applied by the different modeling teams derived from the interpretative modeling of the Step 3 fault activation experiment.

Input parameters		Unit	ENSI		LBNL 3DEC	
			Minor Fault	Fault-core Interface	Minor Fault	Fault-core Interface
Fault	Normal stiffness	GPa/m	84	20	100	100
	Cohesion	MPa	0.85	0.85	0.5	0.5
	Friction angle	°	22	22	22	22
	Dilation angle	°	0	10	11	11
	creation aperture	μm	28	28	28	28
	Fault Dip	°	30	60	37	60
Initial stress	σ_v	MPa	5.5		5.5	
	σ_H	MPa	4.7		4.7	
	σ_h	MPa	4.2		3.8	

terms of shear and normal displacement on the main N50°E and dipping 61°SE fault plane. A larger shear slip of ~300 μm is observed in the LBNL data, compared to the ENSI results. Nevertheless, this calculated slip still underestimates the in situ one which is about 850 μm (Fig. 13). The LBNL model reproduces reasonably well the complex opening – closing observed in the field. As mentioned before, this event is explained by the additional plane considered in the LBNL model. Comparison between these two models thus highlights the strong effect of the fault zone structural complexity on the local displacement measurements. Both models reasonably well reproduce the activation of the fault as a normal fault. The LBNL model which considers an additional local complexity much better reproduces both the magnitudes of displacements and the injected flowrate showing the strong effect of a local complexity on fault leakage. This is also the reason why the LBNL model is stopped earlier that the ENSI's one. A leakage flow path preferentially formed along that structure that fast reached the boundaries of the model. Main reason for that is that this structure although secondary is favorable oriented for shear than the main fault.

7. Discussion

In the following we discuss the overall model comparison and parameters (Section 7.1), the relevance of the findings to the performance

assessment of a nuclear waste repository (Section 7.2), and finally we discuss more advanced fault friction models that were not applied in this model comparison study (Section 7.3).

7.1. Overall model comparison and key parameters

The different numerical simulators and fault hydromechanical models applied in this study were all able to model the hydromechanical behavior observed in the field with reasonable accuracy. These include hydromechanical models that are fully coupled or sequentially coupled, and models with fault behavior represented by either an interface or by finite thickness solid elements. The hydromechanical behavior of the fault was represented best when modeling a propagating rupture along an existing weakness plane (that has very low initial permeability) which causes sudden permeability increases, simulated by an aperture opening or damage enhancing factor. Such models capture the observed behavior of abrupt flow increase when pressure increases over the pressure required to propagate the rupture, and the subsequent flow decrease once the injection pressure is lowered below a threshold pressure to hydraulically close the fracture.

The model parameters applied by the various teams are realistic; in many cases these are based on and agree reasonably well with the best estimates of properties of Opalinus Clay from the site investigations at the Mont Terri laboratory.[54,55] As mentioned, the timing of the rupture for both Step 2 and Step 3 experiments was captured by balancing the applied shear strength and shear stress on the fault. While all teams used the same values of friction angle there were some differences in the cohesion and applied shear stress. The applied shear stress is determined by the dip of the modeled discontinuities and by the values σ_V and σ_H, which vary significantly for the different models. This indicates a degree of non-uniqueness of the calibrated parameters.

It is relevant to compare the stress input applied by the different teams with estimates of the Mont Terri stress field, such as given in the comprehensive analysis of Corkum and Martin[54], who reviewed previous stress measurements and suggested σ_V = 6–7 MPa and σ_H = 4–5 MPa, leading to a differential stress (σ_V - σ_H) averaging 2 MPa. While ENSI and LBNL-TOUGH applied a stress field within this range with a differential stress of 1.8 MPa for modeling the Step 2 experiment (Table 3), other teams applied a stress field with much less difference, ranging from 0.1 to 1.0 MPa. A low stress difference was necessary in some cases to prevent too early shear failure and too large shear slip magnitude. ENSI and LBNL-TOUGH could appy σ_V and σ_H within the range of estimates of Corkum and Martin[46] by impeding shear through a
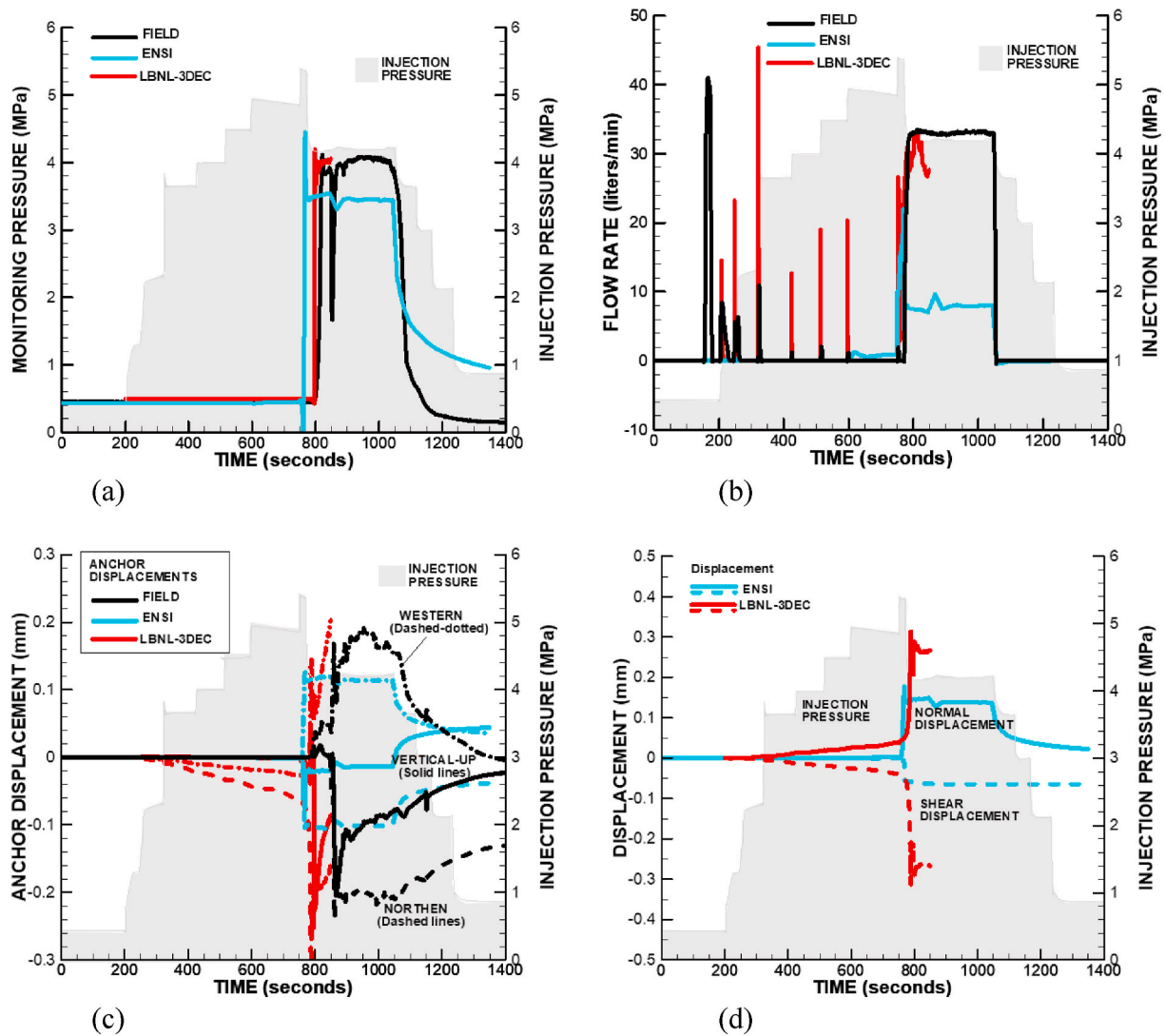
Fig. 15. Comparison of modeling results with field data for the Step 3 fault activation experiment with the controlled injection pressure in gray shade and field data in black. (a) Injection flow rate, (b) pressure at P2, (c) anchor displacements at the monitoring point, and (d) fracture normal and shear displacement at the monitoring point. (For interpretation of the references to colour in this figure legend, the reader is referred to the Web version of this article.)

higher cohesion value.

Finally, for the Step 3 models, both ENSI and LBNL-3DEC applied a stress field of $\sigma_V = 5.5$ MPa and $\sigma_H = 4.2$ MPa, therefore with a vertical stress below the 6–7 MPa range estimated from previous studies. In fact, Guglielmi et al.[13] performed a detailed analysis of the displacement responses at the injection borehole to back-calculate the stress field, which indicated that the smaller value of 5.5 MPa is a better estimate for the test location. It is possible that this could reflect a stress disturbance around the Mont Terri Main Fault, leading to slightly different stress compared to the general stress field at Mont Terri. Note that the Step 3 experiment was conducted well within the damage zone of the fault, and close to a section where the fault core bends, meaning that the maximum principal stress may not be exactly vertical as has been assumed in the current models of DECOVALEX-2019 Task B. Models in step 3 also highlighted the importance to choose the model complexity that best represents the fault zone in order to get a relevant estimation of both fault displacement and flow rate.

7.2. Relevance to repository performance

In the performance assessment of a repository, the evolution of the isolation barriers should be estimated.[60] In this case we have to estimate

the evolution of the host rock barrier function. As illustrated in Fig. 1, thermo-poroelastic stress changes may lead to hydraulic fracturing or shear activation of faults and fractures that may impact the host rock barrier function. These processes have to be considered in the thermal management and repository design.[61]

We found that certain input parameters impact different processes and events during the Mont Terri fault activation experiments. In Table 5 we relate these key parameters and events to the repository performance associated with the sealing capacity of the host rock barrier. We found that the timing of the shear activation was determined by the balance between the shear stress acting on the fault and its shear strength. The key parameters for the balance between shear stress and strength include the three dimensional in situ stress field, the orientation of the fault or fractures relative to the principal stresses, and the shear strength of the fault (cohesion and friction angle). On top of this, the thermo-poroelastic stress changes and their impact on fault shear stress and shear strength will have to be estimated.

Accurate determination of the initial three-dimensional stress field will be critical for predicting when a fault could be reactivated or when more wide spread activation of fractures could occur. As experienced from the Mont Terri site, stress determination in claystone is difficult and there could be significant uncertainty in the estimate of the three-

Table 5

Key parameters and their relevance for predicting repository barrier performance based on their impact on the experimental response during the Mont Terri fault activation experiments.

Parameters	Experimental response	Relevance for repository barrier performance
Fracture normal stiffnes	Impacted initial elastic opening and peak injection rate	Impacts fracture permeability and flow especially during high over pressure by thermal pressurization or gas generation
Cohesion and friction angle	Affected the timing of shear activation	Shear strength parameters that are important for predicting when a fault could be activated or when more widespread shear activation of fractures can take place in the host rock.
Dilation angle	Had an impact only in cases of large shear such as at the monitoring well in the Step 3 test.	Important for how much permeability might change due to shear and therefore potential permanent permeability enhancement
Fracture creation aperture	Permeability increase and peak injection rate and provided for an abrupt pressure response at monitoring wells	Results in a damage induced permeability increase due to fracture creation that may remain after overpressure is reduced.
Fault or fracture Orientation	Adopted fault dip affected shear and normal stress across the fault, which in turn impacted the timing of shear activation	Critical for determine if a fault or fracture will be activated in shear or tensile opening or a combination thereof
Principal stress magnitudes and orientation	Adopted stress field, affected initial normal and shear stress on the fault and therefore the timing of shear activation.	Critical for determine if a fault or fracture will be activated in shear or tensile opening or a combination thereof

dimensional stress field, especially related to the magnitudes of the principal stresses.[58] Model parameters such as friction angle and cohesion can be estimated based on laboratory tests on rock cores from the site such as have been done at the Mont Terri Laboratory.[55] Finally, if fractures and faults are activated, the potential changes in permeability depends of whether the fractures dilate and open during shear, or if they rather compact without any significant permeability increase. The modeling of the field tests in this study showed that most significant permeability change occurred when fluid pressure approached and exceeded the estimated initial stress normal to the opened fractures. However, as soon as the pressure was reduced to about 1–2 MPa less than the estimated normal stress, injection rate declined to close to zero indicating hydraulic closure. The fact that the activated discontinuity closes as soon as the pressure decreases provides an important and beneficial feature for nuclear waste disposal in argillaceous clays, i.e., demonstrating a self-sealing mechanism which keeps the host rock barrier tight and limits the longevity of transport pathways.

This study demonstrates how these types of in situ experiments can be used to evaluate potential permeability changes and the self-sealing performance. The tests can provide for an in situ determination of fracture and fault properties not impacted by sample disturbance. Moreover, these in situ characterization tests can also be used to better constrain the three-dimensional stress field.[15,24]

7.3. Consideration of advanced fault friction models

The modeling performed in this study could reproduce the overall hydromechanical responses observed from the experiments using basic constitutive models, such as the Coulomb criterion, a linear normal stiffness, and the cubic law for fracture flow. The models were sufficient to model observed elastic opening and shear activation of the fault, the

abrupt changes in injection rate, as well as hydraulic closure when the injection pressure was reduced. However, a more detailed examination of the different stages of the field data reveals more complex behavior. For example, Park et al.[22] examined the benchmark cases under slightly different stress conditions and found an initial stable shear slip event prior to the main shear slip. Moreover, Guglielmi et al.[14] examined in detail the transient fault displacement evolution of the Step 3 experiment and identified a small slow slip event. Such slow slip events have been observed in the past at similar field experiments.[56] The phenomena of stable to unstable slip have been quite extensively studied and modeled with slip weakening models,[19,41,62,63] or with rate-and-state friction models.[33,64,65] This is related to an aseismic to seismic slip transition in which rupture extent and the stress transfer from asseismic slip at the center can drive the seismic front at the edges of the rupture zone.[63,66] A rate frictional law combined with a rate-and-state permeability law have also been applied for reproducing some of the complex behavior at the Mont Terri fault activation experiments.[67] This is an active research area which to a large part has been triggered by the need for a better understanding of induced seismicity mechanisms associated with underground injection activities. One questions is whether such complex fault constitutive models are necessary for the performance assessment related to nuclear waste repository; simplified models for bounding estimates of possible changes to the sealing barriers may be sufficient. However, subtle aseismic changes in permeability as have been observed in some of the Mont Terri experiments may be relevant and should be assessed over the long-term repository performance period.

8. Conclusions

Overall, this DECOVALEX-2019 task has (1) resulted in important model developments and adaptations of numerical simulators to simulate fault activation and (2) provided an increased understanding of the hydromechanical behavior of minor faults and fractures in low-permeability shale formations. Two different injection experiments which activated discontinuities within the Mont Terri Main Fault, including parts of the damage zone and close to the fault core, were successfully modeled by a variety of research teams. The key for accurately representing these two activation experiments is a hydromechanical fault model that captures the abrupt activation behavior. The first characteristic of this activation behavior is a sudden increase in fracture permeability and flow rate along with a rupture propagation that is triggered at a certain injection pressure magnitude higher than the estimated stress normal to the discontinuity. The second characteristic is a sudden hydraulic closure of the discontinuity that occurs when the injection fluid pressure is reduced to about 1–2 MPa less than the stress normal to the fault. This behavior was modeled by permeability enhancement resulting from damage induced plastic failure and a subsequent permeability reduction as a result of elastic fracture closure. The fact that the activated discontinuity closes as soon as the pressure decreases provides an important and beneficial feature for nuclear waste disposal in argillaceous clays, i.e., demonstrating a self-sealing mechanism which keeps the host rock barrier tight and limits the longevity of transport pathways. The models developed and tested within this DECOVALEX task can now be applied to predict such behavior at a repository site in an argillaceous claystone, but the hydromechanical fault activation models would ideally be tested and validated by site specific experiments of the type conducted and analyzed in this task.

Declaration of competing interest

The authors declare that they have no known competing financial interests or personal relationships that could have appeared to influence the work reported in this paper.

Acknowledgment

References

1 Rutqvist J, Tsang C-F. A study of caprock hydromechanical changes associated with CO2 injection into a brine aquifer. *Environ Geol*. 2002;42:296–305.
2 Davies R, Foulger G, Bindley A, Styles P. Induced seismicity and hydraulic fracturing for the recovery of hydrocarbons. *Mar Petrol Geol*. 2013;45:171–185.
3 Flewelling SA, Tymchak MP, Warpinski N. Hydraulic fracture height limits and fault interactions in tight oil and gas formations. *Geophys Res Lett*. 2013;40:3602–3606.
4 Lei X, Huang D, Su J, et al. Fault reactivation and earthquakes with magnitudes of up to Mw4.7 induced by shale-gas hydraulic fracturing in Sichuan Basin, China. *Sci Rep*. 2017;7971. https://doi.org/10.1038/s41598-017-08557-y.
5 Urpi L, Rinaldi AP, Rutqvist J, Wiemer S. Fault stability perturbation by thermal pressurization and stress transfer around a deep geological repository in a clay formation. *J Geophys Res: Solid Earth*. 2019;124:8506–8518. https://doi.org/10.1029/2019JB017694.
6 Ghabezloo S, Sulem J. Stress dependent thermal pressurization of a fluid-saturated rock. *Rock Mech Rock Eng*. 2009;42:1–24. https://doi.org/10.1007/s00603-008-0165-z.
7 Seyedi D.M., Plúa C., Vitel1 M., Armand G, Rutqvist J., Birkholzer J., Xu H., Guo R., Thatcher K., Bond A.E., Wang W., Nagel T., Shao H., Kolditz O. Upscaling THM modelling from small-scale to full-scale in-situ experiments in the Callovo-Oxfordian claystone. Int J Rock Mech Min Sci (this issue, submitted March 2020).
8 Rutqvist J, Zheng L, Chen F, Liu H-H, Birkholzer J. Modeling of coupled thermo-hydro-mechanical processes with links to geochemistry associated with bentonite-backfilled repository tunnels in clay formations. *Rock Mech Rock Eng*. 2014;47:167–186.
9 Ortiz L, Volckaert G, Mallants D. Gas generation and migration in Boom Clay, a potential host rock formation for nuclear waste storage. *Eng Geol*. 2002;64:287–296. https://doi.org/10.1016/S0013-7952(01)00107-7.
10 Zhu G-A, Dou L-M, Liu Y, et al. Dynamic behavior of fault slip induced by stress waves. *Shock Vib*. 2016. https://doi.org/10.1155/2016/4386836. Article ID 4386836.
11 Barbour AJ. Pore pressure sensitivities to dynamic strains: observations in active tectonic regions. *J. Geophys. Res. Solid Earth*. 2015;120:5863–5883.
12 Brodsky EE, Van der Elst NJ. The uses of dynamic earthquake triggering. *Annu Rev Earth Planet Sci*. 2014;42:317–339.
13 Guglielmi Y, Birkholzer J, Rutqvist J, Jeanne P, Nussbaum C. Can fault leakage occur before or without reactivation? Results from an in situ fault reactivation experiment at Mont Terri. *Energy Procedia*. 2017;114:3167. https://doi.org/10.1016/j.egypro.2017.03.1445, 31.
14 Guglielmi Y, Nussbaum C, Jeanne P, Rutqvist J, Cappa F, Birkholzer J. Complexity of fault rupture and fluid leakage in shale: insights from a controlled fault activation experiment. *J Geophys Res: Solid Earth*. 2020;125, e2019JB017781. https://doi.org/10.1029/2019JB017781.
15 Guglielmi Y, Nussbaum C, Jeanne P, Rutqvist J, Cappa F, Birkholzer J. Estimating perturbed stress from three-dimensional borehole displacements induced by fluid injection in fractured or faulted shales. *Geophys J Int*. 2020;221:1684–1695. https://doi.org/10.1093/gji/ggaa103.
16 Birkholzer JT, Tsang CF, Bond AE, Hudson JA, Jing L, Stephansson O. 25 years of DECOVALEX - scientific advances and lessons learned from an international research collaboration in coupled subsurface processes. *Int J Rock Mech Min Sci*. 2019;122:103995.
17 Graupner B, Rutqvist J, Guglielmi Y. *DECOVALEX-2019 Task B Final Report*. Lawrence Berkeley National Laboratory, LBNL-2001263d; 2020.
18 Guglielmi Y, Cappa F, Lanc H, et al. ISRM suggested method for step-rate injection method for fracture in-situ properties (SIMFIP): using a 3-component Borehole Deformation Sensor. *Rock Mech Rock Eng*. 2014;47:303–311.
19 Zhang X, Jeffrey RG, He C. A numerical model for the effect of permeability change on faulting during fluid injection. *J Geophys Res: Solid Earth*. 2019;124:2080–2101. https://doi.org/10.1029/2018JB016073.
20 Hu M, Rutqvist J. Numerical manifold method modeling of coupled processes in fractured geological media at multiple scales. *J Rock Mech Geotech Eng*. 2020;12:667–681.
21 Yina Z, Huang H, Zhang F, Zhang L, Maxwell S. Three-dimensional distinct element modeling of fault reactivation and induced seismicity due to hydraulic fracturing injection and backflow. *J Rock Mech Geotech Eng*. 2020;12:752–767.
22 Park J-W, Guglielmi Y, Graupner B, Rutqvist J, Park E-S, Lee C. Modeling of fluid injection-induced fault reactivation using coupled fluid flow and mechanical interface model. *Int J Rock Mech Min Sci*. 2020;132, 104373. https://doi.org/10.1016/j.ijrmms.2020.104373.
23 Watanabe N, Wang W, Taron J, Görke UJ, Kolditz O. Lower dimensional interface elements with local enrichment: application to coupled hydro-mechanical problems in discretely fractured porous media. *Int J Numer Methods Eng*. 2012;90:1010–1034. https://doi.org/10.1002/nme.3353. URL wileyonlinelibrary.com.
24 Shiu W., Guglielmi Y., Graupner B., Rutqvist J. Modelling the water injection induced fault slip and its application to in-situ stress estimation. Int J Rock Mech Min Sci (this issue, submitted, April 2020).
25 Witherspoon PA, Wang JSY, Iwai K, Gale JE. Validity of cubic law for fluid flow in a deformable rock fracture. *Water Resour Res*. 1980;16:1016–1024.
26 Zimmerman RW, Bodvarsson GS. Hydraulic conductivity of rock fractures. *Transport Porous Media*. 1996;23:1–30.
27 Rutqvist J, Leung C, Hoch A, Wang Y, Wang Z. Linked multicontinuum and crack tensor approach for modeling of coupled geomechanics, fluid flow and transport in fractured rock. *Int J Rock Mechanics and Geotech Eng*. 2013;5:18–31.
28 Gan Q, Elsworth D. A continuum model for coupled stress and fluid flow in discrete fracture networks. *Geomech. Geophys Geoenerg. Georesour*. 2016;2:43–61.
29 Hu M, Wang Y, Rutqvist J. Development of a discontinuous approach for modeling fluid flow in heterogeneous media using the numerical manifold method. *Int J Numer Anal Methods GeoMech*. 2015;39:1932–1952.
30 Hu M, Rutqvist J, Wang Y. Fully coupled hydro-mechanical numerical manifold modeling of porous rock with dominant fractures. *Acta Geotechnica*. 2017;12:231–252.
31 Nguyen TS, Guglielmi Y, Graupner B, Rutqvist J. Mathematical modelling of fault reactivation induced by water injection. *Mineral*. 2019;9:282. https://doi.org/10.3390/min9050282.
32 Urpi L, Graupner B, Wang W, Nagel T, Rinaldi AP. Hydro-mechanical fault modelling based on elasto-plasticity with weakness planes. *Int J Rock Mechanics and Geotech Eng*. 2020;12(4):877–885. https://doi.org/10.1016/j.jrmge.2020.06.001.
33 Jha B, Juannes R. Coupled multiphase flow and poromechanics: a computational model of pore pressure effects on fault slip and earthquake triggering. *Water Resour Res*. 2014;50:3776–3808. https://doi.org/10.1002/2013WR015175.
34 Tang XH, Rutqvist J, Hu M, Rayudu NM. Modeling three-dimensional fluid-driven propagation of multiple fractures using TOUGH-FEMM. *Rock Mech Rock Eng*. 2019;52:611–627. https://doi.org/10.1007/s00603-018-1715-7.
35 Rutqvist J, Wu Y-S, Tsang C-F, Bodvarsson G. A modeling approach for analysis of coupled multiphase fluid flow, heat transfer and deformation in fractured porous rock. *Int J Rock Mech Min Sci*. 2002;39:429–442.
36 Rutqvist J. An overview of tough-based geomechanics models. *Comput Geosci*. 2017;108:56–63. https://doi.org/10.1016/j.cageo.2016.09.007.
37 Pruess K, Oldenburg C, Moridis G. *TOUGH2 User's Guide Version 2.1, Report LBNL-43134*. Berkeley, CA, USA: Lawrence Berkeley National Laboratory; 2012.
38 Itasca. *FLAC3d v5.0, Fast Lagrangian Analysis of Continua in 3 Dimensions*. User's Guide; 2011.
39 Rutqvist J, Birkholzer J, Cappa F, Tsang C-F. Estimating maximum sustainable injection pressure during geological sequestration of CO2 using coupled fluid flow and geomechanical fault-slip analysis. *Energy Convers Manag*. 2007;48:1798–1807.
40 Rutqvist J, Rinaldi AP, Cappa F, et al. Fault activation and induced seismicity in geologic carbon storage - lessons learned from recent modeling studies. *J Rock Mech Geotech Eng*. 2016;8:775–966.
41 Rutqvist J, Rinaldi AP, Cappa F, Moridis GJ. Modeling of fault activation and seismicity by injection directly into a fault zone associated with hydraulic fracturing of shale-gas reservoirs. *J Petrol Sci Eng*. 2015;127:377–386.
42 Rinaldi AP, Rutqvist J. Joint opening or hydroshearing? Analyzing a fracture zone stimulation at Fenton Hill. *Geothermics*. 2019;77:83–98.
43 Zbinden D, Rinaldi AP, Urpi L, Wiemer S. On the physics-based processes behind production-induced seismicity in natural gas fields. *J. Geophys. Res. Solid Earth*. 2017;122:3792.
44 Wang W, Kolditz O. Object-oriented finite element analysis of thermo-hydro-mechanical (THM) problems in porous media. *Int J Numer Methods Eng*. 2007;69(1):162–201.
45 Kolditz O, Bauer S, Bilke L, et al. OpenGeoSys: an open-source initiative for numerical simulation of thermo-hydro-mechanical/chemical (THM/C) processes in porous media. *Environ. Earth Sci*. 2012;67(2):589–599.
46 Yoshioka K, Parisio F, Naumov D, Lu R, Kolditz O, Nagel T. Comparative verification of discrete and smeared numerical approaches for the simulation of hydraulic fracturing. *GEM-Int J Geomathemath*. 2019;10(1):13.
47 Cundall PA. Formulation of a three-dimensional distinct element model – Part I: a scheme to detect and represent contacts in a system composed of many polyhedral blocks. *Int J Rock Mech Min Sci Geomech Abstr*. 1988;25:107–116.

48 Itasca Consulting Group Inc. *3DEC – 3-Dimensional Distinct Element Code, Ver. 5.0. 4*. Minneapolis: Itasca: Itasca Consulting Group, Inc.; 2013.

49 Yoon JS, Zang A. Project Final Report. *3D Thermo-Mechanical Coupled Modeling of Thermo-Seismic Response of a Fractured Rock Mass Related to the Final Disposal of Spent Nuclear Fuel and Nuclear Waste in Hard Rock*. vol. 15. Sweden: Swedish Radiation Safety Authority; 2019.

50 Itasca Consulting Group. *Inc. PFC — Particle Flow Code in 2 and 3 Dimensions*. Minneapolis: Itasca; 2019. Documentation Set of version 6.00.12 [April 7 Version 6.0.

51 Yoon JS, Stephansson O, Zang A, Min KB, Lanaro F. Discrete bonded particle modelling of fault activation near a nuclear waste repository site and comparison to static rupture earthquake scaling laws. *Int J Rock Mech Min Sci*. 2017;98:1–9.

52 Jaeger JC, Cook NGW, Zimmerman RW. *Fundamentals in Rock Mechanics*. fourth ed. Oxford: Blackwell publishing; 2007.

53 COMSOL., COMSOL. *Multiphysics®*. Stockholm, Sweden: COMSOL AB; 2020. www.comsol.com.

54 Corkum AG, Martin CD. Modelling a mine-by test at the Mont Terri rock laboratory, Switzerland. *Int J Rock Mech Min Sci*. 2007;44:846–859.

55 Bock, H. RA reportExperiment - Updated Review of the Rock Mechanics Properties of the Opalinus Clay of the Mont Terri URL Based on Laboratory and Field Testing, Technical Report TR 2008-04, Mont Terri Project Underground Rock Laboratory.

56 Guglielmi Y, Elsworth D, Cappa F, et al. In Situ observations on the coupling between hydraulic diffusivity and displacements during fault reactivation in shales. *J Geophys Res: Solid Earth*. 2015;120:7729–7748.

57 Martin CD, Lanyon GW. Measurement of in-situ stress in weak rocks at Mont Terri rock laboratory, Switzerland. *Int J Rock Mech Min Sci*. 2003;40(7–8):1077–1088.

58 Doe T, Vietor T. *DS (Determination of Stress) Experiment: Review of in Situ Stress Measurements and Their Context*. Switzerland: Wabern; 2015. Synthesis report, Mont Terri Technical Report TR 2012-06. Federal Office of Topography (swisstopo) www.mont-terri.ch.

59 Amann F, LeGonidec Y, Senis M, et al. Analysis of acoustic emissions recorded during a mine-by experiment in an underground research laboratory in clay shales. *Int J Rock Mech Min Sci*. 2018;106:51–59.

60 IAEA., INTERNATIONAL ATOMIC ENERGY AGENCY. *Spent Fuel and High Level Waste: Chemical Durability and Performance*. Technical Reports Series No. 413. Vienna: IAEA; 2007.

61 Rutqvist J. Thermal management associated with geologic disposal of large spent nuclear Fuel canisters in tunnels with thermally engineered backfill. *Tunn Undergr Space Technol*. 2020;102, 103454. https://doi.org/10.1016/j.tust.2020.103454.

62 Azad M, Garagash DI, Satish M. Nucleation of dynamic slip on a hydraulically fractured fault. *J Geophys Res: Solid Earth*. 2017;122:2812–2830. https://doi.org/10.1002/2016JB013835.

63 Ciardo F, Lecampion B. Effect of Dilatancy on the transition from aseismic to seismic slip due to fluid injection in a fault. *J Geophys Res: Solid Earth*. 2019;124:3724–3743. https://doi.org/10.1029/2018JB016636.

64 Segall P, Lu S. Injection-induced seismicity: poroelastic and earthquake nucleation effects. *J Geophys Res Solid Earth*. 2015;120:5082–5510.

65 McClure MW, Horne RN. Investigation of injection-induced seismicity using a coupled fluid flow and rate/state friction model. *Geophysics*. 2011;76:WC181. https://doi.org/10.1190/geo2011-0064.

66 Wynants-Morel N, Cappa F, De Barros L, Ampuero J-P. Stress perturbation from aseismic slip drives the seismic front during fluid injection in a permeable fault. *J Geophys Res: Solid Earth*. 2020;125, e2019JB019179. https://doi.org/10.1029/2019JB019179.

67 Jeanne P, Guglielmi Y, Rutqvist J, Nussbaum C, Birkholzer J. Permeability variations associated with fault reactivation in a claystone formation investigated by field experiments and numerical simulations. *J Geophys Res*. 2018;123:1694–1710. https://doi.org/10.1002/2017JB015149.